

## X-RAY SUBSTRUCTURE STUDIES OF FOUR GALAXY CLUSTERS USING *XMM-NEWTON* DATA\*

YU-YING ZHANG<sup>1</sup>, THOMAS H. REIPRICH<sup>1</sup>, ALEXIS FINOGENOV<sup>2,3</sup>, DANIEL S. HUDSON<sup>1</sup>, AND CRAIG L. SARAZIN<sup>4</sup>

<sup>1</sup> Argelander Institut für Astronomie, Universität Bonn, Auf dem Hügel 71, 53121 Bonn, Germany

<sup>2</sup> Max-Planck-Institut für extraterrestrische Physik, Giessenbachstraße, 85748 Garching, Germany

<sup>3</sup> University of Maryland, Baltimore County, 1000 Hilltop Circle, Baltimore, MD 21250, USA

<sup>4</sup> Department of Astronomy, University of Virginia, P.O. Box 400325, Charlottesville, VA 22904, USA

Received 2009 March 2; accepted 2009 May 1; published 2009 June 19

### ABSTRACT

Mahdavi et al. find that the degree of agreement between weak lensing and X-ray mass measurements is a function of cluster radius. Numerical simulations also point out that X-ray mass proxies do not work equally well at all radii. The origin of the effect is thought to be associated with cluster mergers. Recent work presenting the cluster maps showed an ability of X-ray maps to reveal and study cluster mergers in detail. Here, we present a first attempt to use the study of substructure in assessing the systematics of the hydrostatic mass measurements using two-dimensional (2D) X-ray diagnostics. The temperature map is uniquely able to identify the substructure in an almost relaxed cluster which would be unnoticed in the intracluster medium electron number density and pressure maps. We describe the radial fluctuations in the 2D maps by a cumulative/differential scatter profile relative to the mean profile within/at a given radius. The amplitude indicates  $\sim 10\%$  fluctuations in the temperature, electron number density, and entropy maps, and  $\sim 15\%$  fluctuations in the pressure map. The amplitude of and the discontinuity in the scatter complement 2D substructure diagnostics, e.g., indicating the most disturbed radial range. There is a tantalizing link between the substructure identified using the scatter of the entropy and pressure fluctuations and the hydrostatic mass bias relative to the expected mass based on the  $M-Y_X$  and  $M-M_{\text{gas}}$  relations particularly at  $r_{500}$ . *XMM-Newton* observations with  $\sim 120,000$  source photons from the cluster are sufficient to apply our substructure diagnostics via the spectrally measured 2D temperature, electron number density, entropy, and pressure maps.

*Key words:* cosmology: observations – dark matter – diffuse radiation – galaxies: clusters: general – methods: statistical – surveys – X-rays: galaxies: clusters – X-rays: general

*Online-only material:* color figures

### 1. INTRODUCTION

The robustness of cluster mass estimates has become more and more important as galaxy clusters have been widely used as important cosmology tools (e.g., Ebeling et al. 1998, 2000; Allen et al. 2002; Böhringer et al. 2004; Vikhlinin et al. 2009a, 2009b). Precision cluster cosmology experiments using the mass function are based on accurately calibrated mass–observable scaling relations in terms of their shape, scatter, and evolution (e.g., Vikhlinin et al. 2006; Arnaud et al. 2007). To calibrate the mass–observable scaling relations, the first necessary task is to obtain well understood measurements of the cluster mass and observables (e.g., Böhringer et al. 2007; Zhang et al. 2006, 2008). X-ray measurements provide an important estimate of the cluster mass. With deep X-ray observations from *XMM-Newton* and *Chandra*, one can precisely trace both temperature and electron number density distributions of the intracluster medium (ICM) and thus measure the mass distributions with statistical uncertainties below 15% up to  $r_{500}$  (e.g., Vikhlinin et al. 2006). However, the accuracy of X-ray cluster mass estimates is limited by additional physical processes in the ICM and projection effects. Although the current total cluster mass calibration between two independent approaches, weak lensing and X-ray, shows an agreement (e.g., Mahdavi et al. 2008; Zhang et al. 2008), a radial dependence is found in the ratio of weak

lensing and X-ray mass measurements (e.g., Mahdavi et al. 2008). Such a radial dependence is thought to be due to a bias in the hydrostatic mass estimates (e.g., Nagai et al. 2007).

Cluster merging is one of many effects causing biases in the X-ray mass estimates. Previous results on X-ray cluster maps (e.g., Vikhlinin et al. 2001; Markevitch et al. 2003; Schuecker et al. 2004; Finoguenov et al. 2005) show that clusters are not simple hydrostatic equilibrium systems. Both relaxed and unrelaxed clusters may be affected by additional nonthermal pressure processes. Particularly, merging clusters of galaxies are often not in a hydrostatic equilibrium state. Cluster mergers change the X-ray luminosities and temperatures of clusters, both in a transient sense and in the long term (e.g., Ricker & Sarazin 2001; Poole et al. 2006, 2007), and also dramatically affect the properties of their galaxies (e.g., Sun et al. 2007). The temperature distribution, as an important input in the X-ray mass estimate, can cause biases in the X-ray measured mass distribution. Mergers seriously affect both mass estimates and observables, and thus the scaling relations of galaxy clusters (e.g., Evrard et al. 2008). Elimination of systematic uncertainties from the scaling relation calibration demands that major cluster mergers are identified and effects of major mergers on cluster mass estimates are quantified. Substructure can be used to identify and trace the merging process and the substructure fraction can be used to link the cluster mass systematics with the mass assembly history (e.g., Smith & Taylor 2008).

Substructure studies are enormously important to understand cluster mass estimates and the drivers of the scaling relations. Cluster mergers create disturbances associated with both shocks

\* This work is based on observations made with the *XMM-Newton*, an ESA Science Mission with instruments and contributions directly funded by ESA Member States and the USA (NASA).

and mixing of the stripped gas. As parameters controlling their relative importance, e.g., the viscosity, are not so well constrained (Sijacki & Springel 2006), it is unclear how much each contributes and at which scales each effect dominates. Observationally, we are able to provide better constraints using spatial fluctuations of the temperature, electron number density, entropy, and pressure maps. Observational results can be compared with numerical simulations with different prescriptions to reveal more details of the merging physics.

We aim to perform quantitative substructure studies using X-ray spectrally measured two-dimensional (2D) maps to access the systematic errors in cluster mass measurements due to departures from hydrostatic equilibrium. Substructures in galaxy clusters have been intensely investigated since the *ROSAT* era using the X-ray surface brightness distribution from observations and simulations (e.g., Jones & Forman 1984; Böhringer et al. 2007; Ventimiglia et al. 2008; Piffaretti & Valdarnini 2008). However, substructures are less obvious in the X-ray surface brightness distribution than in the temperature distribution as indicated in, e.g., Jee & Tyson (2009), Riemer-Sorensen et al. (2009), and Andersson et al. (2009). The *Chandra* and *XMM-Newton* telescopes, with their high spatial resolution, conveniently provide us the opportunity to perform substructure studies using also the temperature map. Most such studies derive approximate X-ray temperature maps via X-ray hardness ratio maps (e.g., Fabian et al. 2001, 2002; Churazov et al. 2003; Markevitch et al. 2001, 2005; Finoguenov et al. 2005; Zhang et al. 2005; Forman et al. 2007). An alternative and more reliable way to derive X-ray temperature maps with high precision is to perform a spectral analysis in each spatial bin. This method avoids, for instance, spurious temperature variations due to underlying metallicity variations because the metallicity is determined simultaneously (e.g., Henry et al. 2004; Reiprich et al. 2004, 2009; Belsole et al. 2004; Pratt et al. 2005; Sanderson et al. 2005; Sakelliou & Ponman 2006; Sanders & Fabian 2007; Simionescu et al. 2007; Kapferer et al. 2008).

In this paper, we use the spatial fluctuations in the ICM temperature, electron number density, entropy, and pressure in the 2D maps as substructure indicators and the deviation of the mass–observable data pair from the mass–observable relations of relaxed clusters as an estimate of the mass bias. In Section 2, we describe the key steps in the data reduction, particularly emphasizing the background subtraction. Our technique to measure the spectral temperature is shown in Section 3 and how to derive the 2D maps using the spectral analysis is shown in Section 5, respectively. We briefly describe the mass modeling in Section 4, and show our results based on spectrally measured X-ray 2D maps in Section 6.1. We summarize our conclusions in Section 7. Unless explicitly stated otherwise, we adopt a flat  $\Lambda$ CDM cosmology with the density parameter  $\Omega_m = 0.3$  and the Hubble constant  $H_0 = 70 \text{ km s}^{-1} \text{ Mpc}^{-1}$ . We adopt the solar abundance table of Anders & Grevesse (1989). Confidence intervals correspond to the 68% confidence level. The Orthogonal Distance Regression package (ODRPACK 2.01;<sup>5</sup> e.g., Boggs et al. 1987) taking into account measurement errors on both variables is used for example, to derive correlations between observationally derived parameters. We use Monte Carlo simulations to evaluate the propagation of the errors in the X-ray mass modeling on all quantities of interest.

## 2. DATA REDUCTION

Spectrally measured 2D X-ray maps using most existing techniques require high photon statistics and are only applied to a few very nearby clusters/galaxies (e.g., Henry et al. 2004; Reiprich et al. 2004; Belsole et al. 2004; Pratt et al. 2005; Sakelliou & Ponman 2006; Sanders & Fabian 2007; Simionescu et al. 2007). In most previous studies, a relatively simple blank sky background subtraction was often applied. Therefore, high signal-to-noise ratio (S/N) data are required to avoid large uncertainties caused by the background modeling. These technical limitations make this approach applicable only to targets with extremely good photon statistics, requiring 1–2 orders of magnitude higher exposures than the typical archival data for nearby clusters. It is a challenge to carry out such studies on medium quality data.

A precise background subtraction method could make spectrally measured map analysis possible also for medium quality *XMM-Newton* data to increase the size of the cluster sampling. Snowden et al. (2008) developed a precise background modeling method but only for the MOS data and only to measure the radial temperature profile. We adopted their method and developed an advanced background modeling pipeline, which is applicable to both pn and MOS data and which can be used to measure the spectral temperature for both the radial analysis and the map analysis. It allows us to perform reliable spectral analysis in each spatial bin to derive the X-ray maps, but for clusters with *XMM-Newton* data with  $\geq 120,000$  source counts in total.

The XMMSAS version 7.1.0 software combined with our in-house developed pipeline is used for data reduction.

### 2.1. Data Selection

To demonstrate the robustness of the method and to determine the S/N threshold for such substructure studies, we composed a sample of four clusters showing different morphologies as well as different photon statistics in their *XMM-Newton* data. Four clusters of galaxies are selected from the HIFLUGCS;<sup>6</sup> Reiprich & Böhringer (2002) according to the following criteria. (1) The  $r_{2500}$ <sup>7</sup> fits the *XMM-Newton* field of view (FOV). (2) The photon statistics are sufficient for the map analysis using spectral measurements but varies in a small range which gives 10–60 bins, of which the uncertainty of the spectrally measured temperature in each spatial bin is  $\approx 10\%$ . (3) The background is mildly contaminated by flares. (4) The map analysis has not already been published. The first criterion is important to measure the temperature distribution, and thus to guarantee reliable X-ray mass modeling to derive the mass bias. The second and third criteria are required to guarantee robust X-ray background modeling, particularly in the spectral analysis for the map analysis. In addition, the reason we chose those four clusters with slightly different photon statistics is to test how far from the cluster center and how reliably one can perform substructure studies with a range of data quality. Such an investigation is important to justify the

<sup>6</sup> The HIFLUGCS sample consists of 64 X-ray brightest galaxy clusters in the extragalactic sky. They were selected from the *ROSAT* All-Sky Survey (RASS), irrespective of their morphology, simply applying an X-ray flux limit.

<sup>7</sup>  $r_\Delta$  is the radius within which the density contrast to the critical density is  $\Delta$ .  $M_\Delta$  is the total mass within  $r_\Delta$ . For example, for  $\Delta = 200$ ,  $r_{200}$  is the radius within which the density contrast is 200 and  $M_{200}$  is the total mass within  $r_{200}$ . The  $r_{200}$  used here is derived from the cluster global temperature in Reiprich & Böhringer (2002) and the  $M_{200}$ – $T$  relation from simulations in Evrard et al. (1996).

<sup>5</sup> <http://www.netlib.org/odrpack> and references therein.

**Table 1**  
Cluster Properties and *XMM-Newton* Observations

Name	OBS-ID	Net Exposure (ks)			Mode		X-Ray Centroid (J2000)		$z$	$N_{\text{H}}$ $10^{22} \text{ cm}^{-2}$	$T_{0.2-0.5r_{500}}$ keV	$r_{\text{tr}}$ arcmin
		MOS1	MOS2	pn	pn	R.A.	Decl.					
IIIZw54	0505230401	23.3	22.3	30.3	EFF	03 : 41 : 18.729	+15 : 24 : 13.91	0.0311	0.1470	$2.17 \pm 0.03$	13.35	
A3391	0505210401	23.3	24.6	18.2	EFF	06 : 26 : 24.222	-53 : 41 : 24.02	0.0531	0.0559	$5.02 \pm 0.05$	13.32	
EXO0422	0300210401	31.5	32.2	32.7	EFF	04 : 25 : 51.224	-08 : 33 : 40.34	0.0390	0.0808	$2.99 \pm 0.03$	13.29	
A0119	0505211001	8.2	8.0	7.6	FF	00 : 56 : 17.119	-01 : 15 : 11.98	0.0440	0.0328	$5.47 \pm 0.11$	11.00	

**Notes.** The EFF mode is the extended full frame mode. The MOS data are in FF mode. The truncation radius ( $r_{\text{tr}}$ ) is the radius corresponding to an S/N of 3.

required photon statistics for substructure studies of galaxy clusters using X-ray maps on different levels. Our empirical results will be useful for the community to sample clusters and to perform X-ray observations for such substructure studies. We set the fourth criterion in order to get new scientific results out of our tests.

## 2.2. Data Preparation

To prepare the data, we apply iterative screening using a  $2\sigma$  clipping as described in Zhang et al. (2006, 2007) using both the soft band (0.3–10 keV) and the hard band (10–12 keV for MOS and 12–14 keV for pn) to filter flares. Hereafter, we call those light-curve screened events for the clusters the target observations (TOs). The properties of the four clusters are presented in Table 1.

## 2.3. Point-like Source Identification and Subtraction

The “edetect\_chain” command is used to detect point-like sources. Point sources in the outskirts of the cluster are subtracted. In the cluster center, only these detected point-like sources carefully checked by eye and identified with detected point-like sources in *Chandra* (Hudson et al. 2009) are subtracted.

There is good agreement between *XMM-Newton* and *Chandra* detected central point-like sources. For IIIZw54, a point source is detected by both *XMM-Newton* and *Chandra* at the center (03:41:17.54, +15:23:47.61), where a cD galaxy sits. A3391 also has a point source at the center (06:26:20.45, -53:41:35.80) coincident with the cD, detected by both *XMM-Newton* and *Chandra*. For EXO0422, there are no evident point-like sources detected by *Chandra* at the center. The *XMM-Newton* image shows extremely peaked X-ray emission similar to a point-like source (04:25:51.25, -08:33:36.97) at the position of the cluster galaxy C1G 0422-09 (also see Belsole et al. 2005). Conservatively, we identify it as a point-like source and subtract it. For A0119, there are no evident point-like sources in the cluster center in either *XMM-Newton* or *Chandra* data, cospatial with a cD.

## 2.4. Background Treatment

As also described in Snowden et al. (2008), the following four background components have been taken into account in our background treatment. The first is the quiescent particle background (QPB). The second is the fluorescent X-ray background (FXB). The third is the soft proton-caused background (SPB). The fourth is the cosmic X-ray background (CXB).

### 2.4.1. QPB and FXB

The treatment of the QPB and FXB has been documented using the filter wheel closed (FWC) observations for MOS in Snowden et al. (2008) and for pn in Freyberg et al. (2006).

As a first step to model the QPB and FXB, we extract the spectra using events out of the FOV<sup>8</sup> from the FWC observations<sup>9</sup> to investigate the properties of the QPB and FXB using the 2–12 keV band as done in Snowden et al. (2008) and Freyberg et al. (2006). The FWC MOS1/MOS2 (pn) spectrum can be well fitted by a “powerlaw/b” model together with six (eight) “Gaussian/b” models to account for the FXB lines. The photon index of the “powerlaw/b” model,  $\Gamma$ , is  $0.154 \pm 0.006$  for MOS1 (reduced  $\chi^2 = 1.14$  for 645 degrees of freedom (dof)),  $0.138 \pm 0.008$  for MOS2 (reduced  $\chi^2 = 1.09$  for 645 dof) and  $0.345 \pm 0.012$  for pn (reduced  $\chi^2 = 0.89$  for 630 dof), respectively. The best fit provides reliable measurements of the “LineE” parameter with a few percent precision and of the “Sigma” parameter within a factor of 1.4 for the “Gaussian/b” model. Across the detectors we found the slope of the “powerlaw/b” is  $\sim 0.15$  for MOS and  $\sim 0.35$  for pn, both varying by at most 15%. The properties of the FWC observations are consistent with the results found in de Plaa et al. (2006) and Freyberg et al. (2006).

De Luca & Molendi (2004) pointed out that a simple renormalization of the QPB using the high-energy band (e.g., 8–12 keV) count rate may lead to systematic errors in both the continuum and the lines. We thus checked the out of FOV-extracted spectra of  $\sim 60$  TOs. The slope of the individual TOs is indeed inconsistent (up to  $\sim 50\%$ ) with the stack FWC observations when the full 2–12 keV band is used. A consistency of the slope appears when the 3–10 keV band is fitted. We therefore renormalize the FWC observations for the QPB and FXB subtraction using a broad band of 3–10 keV. The best fit of the photon index ( $\Gamma$ ) of the stack FWC observations using the 3–10 keV band is  $0.144 \pm 0.016$  for MOS1 (reduced  $\chi^2 = 1.07$  for 640 dof),  $0.140 \pm 0.017$  for MOS2 (reduced  $\chi^2 = 1.03$  for 637 dof), and  $0.341 \pm 0.039$  for pn (reduced  $\chi^2 = 0.89$  for 498 dof), respectively.

As a second step, for both MOS and pn, we model and subtract the QPB for individual observations using the stacked FWC observations with the same mode as for the TOs. To determine the normalization, we extract the spectra using events out of the FOV (#XMMEA\_16) and outside of a  $15'.4$  radius from the detector center for both FWC observations and TOs. As De Luca & Molendi (2004) found, both X-ray photons and low-energy particles can reach CCD 2 and CCD 7 of the MOS cameras. We exclude both CCDs for MOS. For later observations with the MOS1 camera, we exclude CCD 6 in the FWC data to match the loss of MOS1 CCD 6 in the TOs. As also found in Snowden et al. (2008), some observations show occasional deviations of CCD 4 and CCD 5 for MOS1 and CCD 5 for MOS2. These CCDs are then excluded as

<sup>8</sup> An expression of “#XMMEA\_16” in the SAS command “evselect” means to select the events out of the FOV.

<sup>9</sup> [http://xmm.vilspa.esa.es/external/xmm\\_sw\\_cal/background/#EPIC](http://xmm.vilspa.esa.es/external/xmm_sw_cal/background/#EPIC)

well for those observations. Freezing the photon index of the “powerlaw/b” model and the “LineE” and “Sigma” parameters of the “Gaussian/b” model to the best fit derived above using all events out of the FOV from the FWC observations in the 3–10 keV, we obtained the normalization from the best fit. The renormalization factor ( $n_{\text{QPB}}$ ) of the continuum component is derived as the “powerlaw/b” normalization ratio of the TO to FWC observations. The FWC spectrum ( $S_{\text{FWC}}$ ) is normalized by this renormalization factor,  $n_{\text{QPB}}$ , and subtracted from the TO spectrum ( $S_{\text{TO}}$ ) for each instrument.

#### 2.4.2. SPB

The screening procedure described in Section 2.2 using both the hard band and the soft band to prepare the data has filtered all of the significant SPB component for most observations. The observations with significant residual SPB found in the spectral analysis shall be excluded. Luckily, none of the observations for the four clusters show significant residual SPB.

#### 2.4.3. CXB

Both RASS data and PSPC pointed data can be used to model the CXB. The latter, of higher statistical quality, are preferred. The *ROSAT* PSPC calibration shows an accuracy of better than 5% even for energies lower than 0.28 keV (Beuermann 2008). Therefore, we use the *ROSAT* PSPC pointed data in the 0.1–2.4 keV band to model the CXB. The spectrum was extracted from the region just beyond  $r_{200}$  for each cluster. The best fit of the spectrum shows that the CXB can be well described by a combined model, “mekal+wabs\*(mekal+powerlaw).” The temperature of the unabsorbed thermal component is often  $\sim 0.1$  keV, and of the absorbed thermal component is often between 0.1 and 0.2 keV, respectively. To avoid large background fluctuations, we have excluded regions showing bright sources identified by eye. The absorbed “powerlaw” model, with its slope set to 1.41, accounts for unresolved point sources (De Luca & Molendi 2004). The “wabs” model is set to the hydrogen column density from the Leiden/Argentine/Bonn (LAB) Galactic H I survey<sup>10</sup> (Hartmann & Burton 1997; Arnal et al. 2000; Bajaja et al. 2005; Kalberla et al. 2005) at the *XMM-Newton* determined cluster center. We repeated the CXB modeling with a “mekal+wabs\*(mekal+mekal+powerlaw)” model, which includes a second absorbed thermal emission component, and which shows no significant improvement of the fit. Therefore, we use the “mekal+wabs\*(mekal+powerlaw)” model for the CXB.

With increasing radial distance from the cluster center, the CXB becomes dominant over the cluster emission. We therefore use the outskirts to model the CXB. We extract the *XMM-Newton* spectra from the outermost region ( $9'.17 < R < 10'$  from the cluster center) in the *XMM-Newton* FOV,  $S_{\text{TO}}$ . The FWC spectrum is extracted from the same detector coordinates as for the TO spectrum, and normalized by  $n_{\text{QPB}}$  (derived in Section 2.4.1). We call these spectra,  $S_{\text{TO}} - n_{\text{QPB}} S_{\text{FWC}}$ , the secondary observational (SO) spectra. To derive the normalization of the CXB and to measure the cluster emission, we made a joint fit of the above *ROSAT* PSPC spectrum by

“mekal+wabs\*(mekal+powerlaw),” and the three *XMM-Newton* EPIC spectra by “wabs\*mekal+mekal+wabs\*(mekal+powerlaw)+powerlaw/b.” Note in this co-fit analysis, we link the temperatures and normalizations of the two “mekal” model and the normalization of the “powerlaw” model for the CXB between *ROSAT* PSPC and *XMM-Newton* EPIC. The first “wabs\*mekal” component in the model for the *XMM-Newton* EPIC spectra takes into account the hydrogen column density absorption (frozen to the value from the LAB survey) and cluster emission with its metallicity fixed to 0.3 solar metallicity. The “powerlaw/b” component takes into account the residual SPB in the *XMM-Newton* spectra, which normalization should be consistent with zero. For some TOs, the “powerlaw/b” normalization can be significantly higher, which is inconsistent with zero. Due to the SPB contamination, the spectra from the corners out of the FOV for such TOs often show completely inconsistent shape (i.e., the slope of the “powerlaw” component) with that for the FWC observations. Therefore, the designed QPB background treatment using the FWC observations will fail for such TOs, and they should not be used for our analysis. Luckily, the normalization of the “powerlaw/b” model for all four clusters is consistent with zero. This confirms that the light-curve screening procedure in Section 2.2 has removed all of the significant flares for these four clusters.

De Luca & Molendi (2004) derived the normalization of 0.00345 photons  $\text{keV}^{-1} \text{cm}^{-2} \text{s}^{-1} \text{deg}^{-2}$  at 1 keV for the “powerlaw” model of the CXB with a photon index of 1.41 using *XMM-Newton* EPIC data. The agreement is better than 40% between their value and the best-fit value from our co-fit of *ROSAT* PSPC pointed data and *XMM-Newton* EPIC data for each annulus for each cluster, i.e., within 28% for IIZw54, within 14% for A3391, within 40% for EXO0422, and within 30% for A0119. And the agreement becomes better with increasing radial distance from the cluster center as the cluster emission becomes less dominant in the outskirts. Setting the normalization to the value in De Luca & Molendi (2004), we observe no pronounced change in the  $\chi^2$  and measured parameters of the best fit. Note that the best fits of the spectra also provide reasonable cluster temperatures in comparison to previous published results.

### 3. SPECTRAL ANALYSIS FOR TEMPERATURE PROFILE

#### 3.1. Point-Spread Function and Vignetting

Using the *XMM-Newton* point-spread function (PSF) calibrations in Ghizzardi (2001), we estimate the redistribution fraction of the flux. It is 20% for bins with widths of about 0.5 and less than 10% for bins with widths  $\geq 1'$  neglecting energy- and position<sup>11</sup>-dependent effects. We thus require annular width  $\geq 0.5$  in the radial spectral analysis. The PSF effect is important within 0.5, which corresponds to  $\leq 0.038 r_{500}$  for our four nearby clusters. The PSF effect introduces an uncertainty only to the radial temperature measurement in the inner bins. We made an attempt to correct for the PSF effect for RXCJ2228 + 2037 in Jia et al. (2008), and found the PSF correction is important mainly in the inner radii and causes effects well within 10% level on the temperature measurements. A similar conclusion was reached in Snowden et al. (2008) for A1795. Therefore, we skip the PSF correction in our radial spectral analysis.

X-ray telescopes often have nonazimuthally symmetric PSFs. In the temperature map, the structure due to effects of the

<sup>10</sup> The LAB survey contains the final data release of observations of  $\lambda 21$  cm emission from Galactic neutral hydrogen over the entire sky, merging the Leiden/Dwingeloo Survey (LDS; Hartmann & Burton 1997) of the sky north of  $\delta = -30^\circ$  with the Instituto Argentino de Radioastronomía Survey (IARS; Arnal et al. 2000; Bajaja et al. 2005) of the sky south of  $\delta = -25^\circ$ . The angular resolution of the combined survey is half-power beamwidth (HPBW)  $\sim 0.6$ . [http://www.astro.uni-bonn.de/~webraai/english/tools\\_labsurvey.php](http://www.astro.uni-bonn.de/~webraai/english/tools_labsurvey.php)

<sup>11</sup> All four observations roughly centered on the cluster centers.

nonazimuthally symmetric PSF might be interpreted as actual structure in the cluster. However, those effects become important only at off-axis radii of larger than  $10'$ . The regions used for our studies are well within an off-axis radius of  $6'$ . Note that the regions used for 2D diagnostics are often  $\leq 6'$  for the four clusters. In addition, these effects are significant only for regions of  $1'$  size along the radial axis in such outer regions. The radial-axis width of the bins are all much larger than  $1'$ , particularly using the *Mask-V* (defined in Section 5.1), in the outer regions.

For both images and spectra, the vignetting is taken into account in the extraction using the “evigweight” created column in the events.

### 3.2. Radial Bin Size

The blank sky accumulations of the archival *XMM-Newton* observations in the Chandra Deep Field-South (CDF-S) can be used as a rough estimate of the background. Note that in the spectral analysis, the background is properly treated as described in Section 2.4. The CDF-S observations are only used as a rough background estimate to determine the radial bin size for the spectral analysis.

We screen the CDF-S observation using the same threshold as for the TOs, and normalize them to the TOs using the hard band (10–12 keV for MOS and 12–14 keV for pn) as described in Zhang et al. (2004). This former step guarantees similar QPB levels, and the latter step guarantees similar SPB levels. The residual SPB and the difference in the CXB and FXB are ignored in the determination of the bin size.

For a cluster with a temperature of  $\sim 4$  keV, the uncertainty in the spectrally measured temperature is  $\leq 5\%$  (10%) using both pn and MOS spectra, giving net source counts of  $\geq 72,000$  (24,000) after the background subtraction. Therefore, the annuli for spectral analysis are determined by requiring (1) that the width of each annulus is larger than  $0.5'$ , (2) that the net source counts is  $\geq C$  per MOS2 spectrum in the 0.5–7.8 keV band. The threshold  $C$  is 18,000 except for the clusters with less than four annuli in total for which  $C$  is 6000. We include an outermost bin which does not fulfill the threshold of  $C$ , with an outer radius truncated to give a maximum net source counts.

### 3.3. Spectral Fitting

To obtain the projected temperature profile, the three EPIC spectra for each annulus are normalized to the solid angle of that annulus taking into account corrections for gaps, bad pixels, and point sources. We performed the background modeling and co-fit as described for the outermost region in Section 2.4.3. Note that we firstly fit the *ROSAT* PSPC spectrum together with one of the *XMM-Newton* EPIC spectrum and found that the fitting parameters (temperature, abundance, and normalization) agree to within a few percent between different EPIC instruments. We then fit the parameters simultaneously to the *ROSAT* PSPC spectrum together with all three *XMM-Newton* EPIC spectra.

To obtain the radial temperature profile for the mass modeling, we deproject the spectra (e.g., Zhang et al. 2007), in which the spectral models for the background components are renormalized to the volume of the radial shell. The deprojected EPIC spectra and *ROSAT* PSPC spectrum are then fitted simultaneously to derive the radial temperature measurements.

## 4. MASS MODELING

The soft band (0.7–2 keV) X-ray surface brightness profile model  $S_X(R)$ , in which  $R$  is the projected radius, is linked to

the ICM electron number density profile  $n_e(r)$  and emissivity function as an integral performed along the line of sight,

$$S_X(R) \propto \int_{-\infty}^{\infty} n_p n_e d\ell. \quad (1)$$

The *XMM-Newton* observed surface brightness profile is derived by subtracting the renormalized (by  $n_{\text{QPB}}$ ) FWC surface brightness profile and the CXB in the 0.7–2 keV band derived in Section 3 from the TO surface brightness profile. The truncation radii ( $S/N \geq 3$ , see Table 1) of the *XMM-Newton* observed surface brightness profiles are rather small ( $< r_{500}$ ). The *ROSAT* observed surface brightness profiles cover radii well beyond  $r_{500}$  with  $S/N \geq 3$ , although with sparse data points in the cluster core. We thus combine the *XMM-Newton* observed surface brightness within its truncation radius ( $r_t$ ) with the *ROSAT* converted observed surface brightness profile<sup>12</sup> beyond  $r_t$  as the observed surface brightness profile (e.g., IIIZw54 in Figure 1). The observed surface brightness profile is fitted by Equation (1) convolved with the *XMM-Newton* PSF matrices to obtain the parameters of the double- $\beta$  model of the electron number density profile,  $n_e(r) = n_{e01}(1 + r^2/r_{c1}^2)^{-3\beta/2} + n_{e02}(1 + r^2/r_{c2}^2)^{-3\beta/2}$ .

We assume that (1) the ICM is in hydrostatic equilibrium within the gravitational potential dominated by dark matter (DM) and (2) the DM distribution is spherically symmetric. The cluster mass is then calculated from the X-ray measured ICM density and temperature distributions by

$$\frac{1}{\mu m_p n_e(r)} \frac{d[n_e(r)kT(r)]}{dr} = -\frac{GM(< r)}{r^2}, \quad (2)$$

where  $\mu = 0.62$  is the mean molecular weight per hydrogen atom.  $k$  is the Boltzmann constant and  $T$  is the temperature. Following the method in Zhang et al. (2007), we use a set of input parameters of the approximation functions, in which  $\beta$ ,  $n_{e0i}$ ,  $r_{ci}$  ( $i = 1, 2$ ) represent the double- $\beta$  electron number density profile  $n_e(r)$  and  $P_i$  ( $i = 1, \dots, 7$ ) represent the deprojected temperature profile  $T(r) = P_3 \exp[-(r - P_1)^2/P_2] + P_6(1 + r^2/P_4^2)^{-P_5} + P_7$  (e.g., for IIIZw54 and EXO0422 in Figure 2), respectively, to compute the mean cluster mass. The mass uncertainties are propagated using the uncertainties of the electron number density and temperature measurements by Monte Carlo simulations as described in Zhang et al. (2007, 2008). The cluster masses  $M_{2500}$  and  $M_{500}$  are used in studying the scaling relations in Section 6.5.

## 5. SPECTRALLY MEASURED 2D MAPS

In our procedure, the 2D temperature, electron number density, entropy, and pressure maps<sup>13</sup> are created based on the spectral measurements in each spatial bin. The binning methods described below allow for less biased definition of the zones

<sup>12</sup> The *ROSAT* converted observed surface brightness profile can be derived using the *ROSAT* surface brightness model in Reiprich & Böhringer (2002) with the following two steps: (1) calculating the electron number density profile from the *ROSAT* surface brightness model using the *ROSAT* emissivity function and (2) projecting the electron number density profile to obtain the *XMM-Newton*-like surface brightness profile using the *XMM-Newton* response and convolving the *XMM-Newton* PSF. In this procedure, the scatter and the error of each bin of the *ROSAT* observed surface brightness profile are propagated.

<sup>13</sup> They will be made publicly available through the German Astrophysical Virtual Observatory (GAVO) under Multivariate Archive of X-Ray Images, <http://www.g-vo.org/MAXI/>.

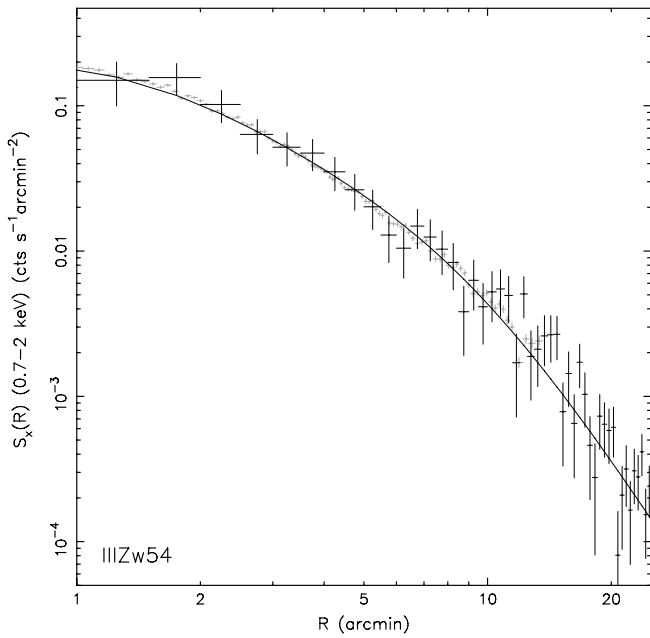


**Figure 1.** Observed surface brightness profile, with the *ROSAT* observed surface brightness profile (black) converted to match the *XMM-Newton* observed surface brightness profile (gray). The continuous curve presents the best fit of the observed surface brightness profile using a double- $\beta$  model for the electron number density profile.

for the spectral extraction compared with the zones determined in the wavelet approach in, e.g., Finoguenov et al. (2005). The available statistics of our data are sufficient to provide detailed 2D diagnostics, and the radial study of the fluctuations for individual clusters—a new complementary tool to measure the substructure.

### 5.1. Mask Determination

We use the MOS2 data to determine the spatial bins in the mask (e.g., for III Zw 54 in Figure 3) for the following two

reasons: (1) the pn data are seriously affected by gaps which can complicate the analysis of cluster structure and (2) the CCD6 is missing for MOS1 for recent observations. We use the 0.5–2 keV band MOS2 image binned in  $4'' \times 4''$  pixels to determine the mask regions for the spectral analysis. The image is binned to give an S/N of  $\geq 33$  for each spatial bin in the mask. For a cluster with a temperature of  $\sim 4$  keV, the uncertainty in the spectrally measured temperature is  $\sim 10\%$  (e.g., for III Zw 54, lower panels in Figure 4).

We adopted two methods to determine the bins (e.g., for II Zw 54 in Figure 3), which are both based on the brightness criteria. One is the weighted Voronoi tessellation method (Cappellari & Copin 2003; Diehl & Statler 2006), whose binning shapes are geometrically unbiased giving a quasi-circle-like shape. This binning scheme is sensitive to local brightness fluctuations (e.g., Simionescu et al. 2007). The other method was developed by Sanders (2006), and bins the brightest pixels of the remaining region. The mask therefore extends along the isophotal annulus centered at the cluster core. This binning scheme is sensitive to the detection of shocks and cold fronts (e.g., Sanders & Fabian 2007). Hereafter, we call the mask defined with the former method as *Mask-V*, and the mask defined with the latter method as *Mask-S*. The advantage of the *Mask-S* binning is that mixing of different temperature components due to a radial temperature gradient is minimal, while the *Mask-V* binning is more sensitive to features like bright spots.

### 5.2. Temperature Maps

The spectra are extracted for each bin in the mask, and normalized to the solid angle of that bin taking into account corrections for gaps, bad pixels, and excluded point sources. The QPB and CXB models derived in Section 3 in the spectral fit are normalized to the solid angle of the bin as frozen models. The MOS and pn spectra are fitted simultaneously by a “wabs\*mekal” model for hydrogen column density absorption and cluster emission, with the frozen models to account for the background. The best-fit temperature and its error bar for each

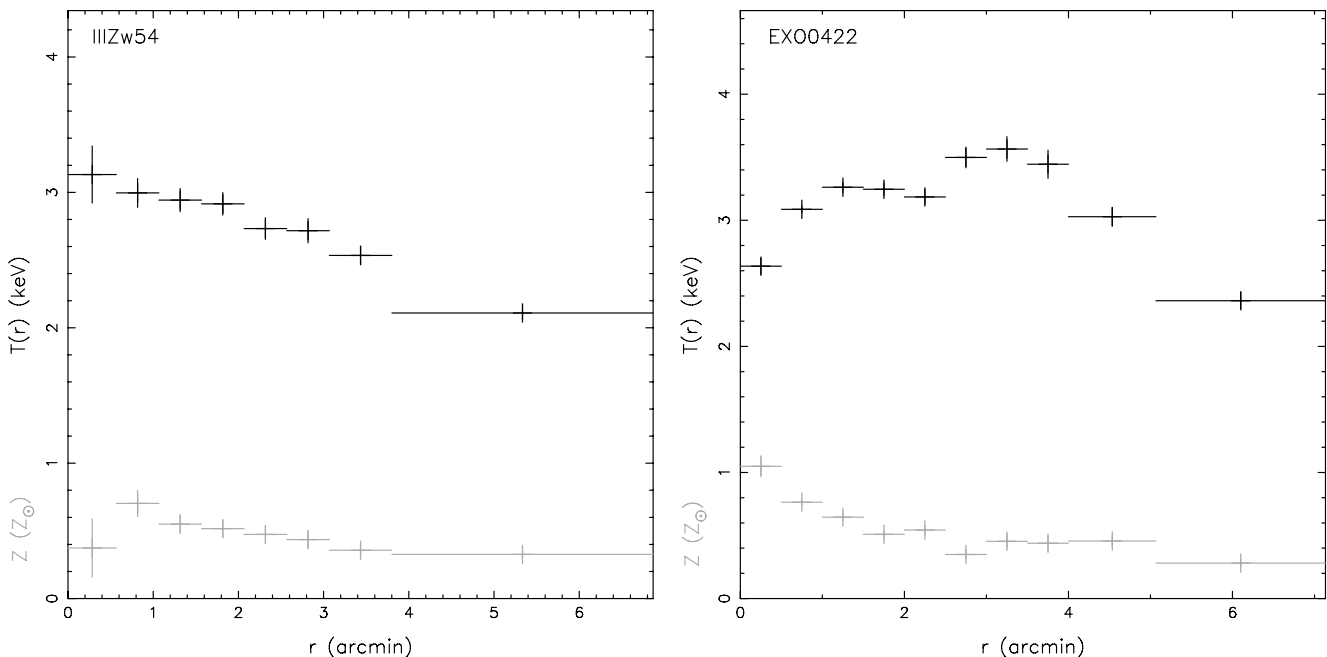


**Figure 2.** Radial (deprojected) temperature (upper) and metallicity (lower) profiles. Note that the very central region ( $r \leq 15''$ ) of EXO0422 was excluded in the spectral analysis to avoid the possible contamination from the galaxy CIG0422-09 found by Belsole et al. (2005).

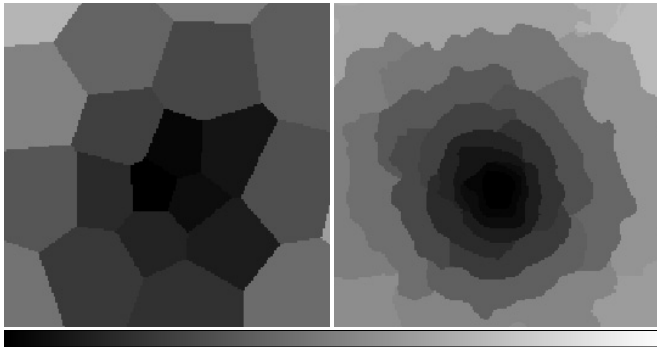


**Figure 3.** Masks using the *Mask-V* (left) and *Mask-S* (right) method for IIZw54. The image size is  $11' \times 11'$ . Each gray scale (from 0 to 34) denotes one bin, but has no physical meaning.

bin are used to create the temperature ( $T$ ) map and its error map (e.g., for IIZw54 shown in Figure 4).

### 5.3. Electron Number Density, Entropy, and Pressure Maps

The spectral normalization in each spatial bin can be used to derive a quasi-deprojected estimate of the electron number density ( $n_e$ ) in that spatial bin (e.g., Henry et al. 2004). In XSPEC, the normalization of the “mekal” model is given as  $K = 10^{-14} / [4\pi D_A^2 (1+z)^2] \int n_e n_H dV$ , where  $D_A$  is the angular diameter distance,  $z$  is the redshift, and the volume corresponding to that spatial bin is approximated by  $V \approx (4/3) D_A^3 \Omega \sqrt{\theta_{\text{out}}^2 - \theta_{\text{in}}^2}$ . Here,  $\Omega$  is the solid angle of the corresponding spatial bin, and  $\theta_{\text{out}}$  and  $\theta_{\text{in}}$  are the angles of the outermost and innermost radii of that bin from the cluster center. As mentioned in Simionescu et al. (2007), it provides a quasi deprojection using an approximation of the three-dimensional extent of each spatial bin and assuming a constant temperature along the line of sight. As most emission in the bin is from the densest gas near the innermost radius of that bin, the electron number density derived from the spectral normalization can be used as the measurement of the electron number density at the projected radius.

The entropy ( $S$ ) and pressure ( $P$ ) maps can be derived from the temperature and electron number density maps by  $S = kTn_e^{-2/3}$  and  $P = kTn_e$ . The X-ray spectrally measured temperature, electron number density, entropy, and pressure maps for IIZw54, A3391, EXO0422, and A0119, respectively, are shown in Figures 5–8.

## 6. SUBSTRUCTURE DIAGNOSTICS WITH ICM $T$ , $n_e$ , $S$ , AND $P$ MAPS

The fluctuations in the 2D maps and their scatter can be used as substructure diagnostics. A disturbance in a cluster may appear as a high amplitude of and/or a discontinuity in the radial profile of the scatter of the fluctuations. Unrelaxed clusters may show larger fluctuations and significant correlations between, e.g., temperature and electron number density fluctuations. The substructure diagnostics of galaxy clusters are therefore directly linked to the scatter of the scaling relations due to the bias in X-ray hydrostatic masses and X-ray observables caused by substructures.

The *Mask-S* method, whose bins are close to radial annuli, has the advantage that the interpretation of a comparison to a mean temperature profile is more straightforward because the range of radii sampled in each bin is smaller. Therefore, we concentrate more on the results from this method, particularly when the data quality is low.

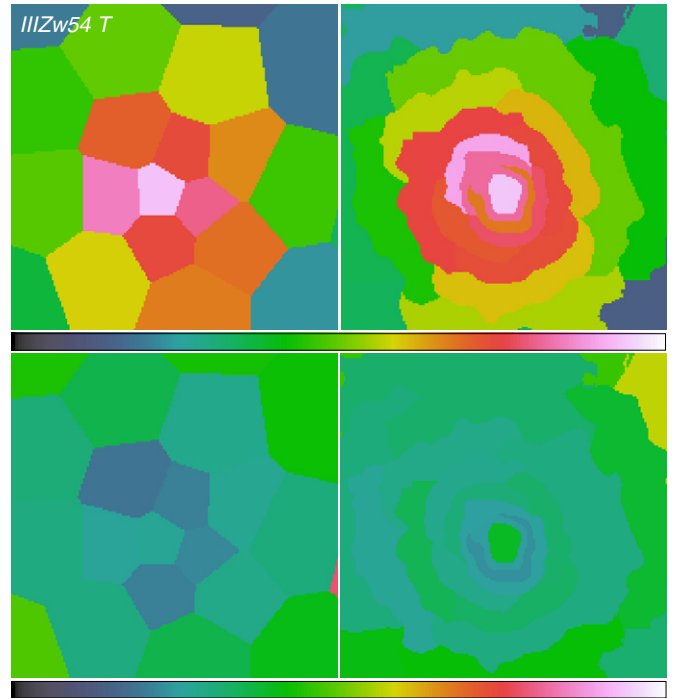


**Figure 4.** Temperature maps (top) and their error maps (bottom) for IIZw54 using *Mask-V* (left) and *Mask-S* (right). The color bar is in the range of 1.5–3.2 keV in the top panels, and 0–0.2 keV in the bottom panels. The image size is  $11' \times 11'$ .

(A color version of this figure is available in the online journal.)

### 6.1. Scatter of the ICM $T$ , $n_e$ , $S$ , and $P$ Fluctuations

The scatter of the fluctuations in the 2D maps from the mean profile can be used as diagnostics of the ICM substructure. Here, we briefly describe how the scatter and error are calculated. To avoid systematic errors due to uncertain background subtraction, we only consider bins of radii  $\leq 0.6r_{\text{tr}}$  ( $r_{\text{tr}}$  see Table 1).

To better show the asymmetries of the clusters, we use a polar coordinate system with the cluster center as its coordinate center. The scaled distribution of a 2D map is defined as  $D(d, \theta)$ , in which  $(d, \theta)$  are the angle and distance in the polar coordinate system. For example  $D(d_i, \theta_i) = T(R_i, \theta_i) / T_{0.2-0.5r_{500}}$  is the value of the 2D spatial bin  $(d_i, \theta_i)$  in a 2D temperature map. Note that  $T_{0.2-0.5r_{500}}$  is the cluster temperature, a volume average of the radial temperature profile limited to the radial range of 0.2–0.5 $r_{500}$  (see Appendix B.2 in Zhang et al. 2008) and  $d_i = R_i / r_{500}$  is the distance between the cluster center and the geometric center of that 2D bin scaled by the cluster  $r_{500}$ . To investigate the asymmetry, we derive an azimuthal-averaged profile  $D(d)$  of the scaled distribution  $D(d, \theta)$ . A nonparametric locally weighted regression<sup>14</sup> (Sanderson et al. 2005, and references therein) of the averaged profile is used to derive the mean profile  $\langle D(d) \rangle$ . The absolute fluctuation distribution is defined as  $F = |D(d, \theta) / \langle D(d) \rangle - A|$ . Here, the renormalization  $A$  is not equal to one only when there is a possible bias in the mean scaled profile. In this work, we used  $A = 1$ . In the scatter calculation, the weighting of the

<sup>14</sup> The procedure calls “lowess” in the R package, which uses locally weighted polynomial regression (e.g., Becker et al. 1988). We used the default smoothing span  $f = 2/3$ . “Local” is defined by the distance to the “floor( $f * n$ )”th nearest neighbor, and tricubic weighting is used for  $x$  which fall within the neighborhood. Note that “floor” in the R package takes a single numeric argument  $x$  and returns a numeric vector containing the largest integers not greater than the corresponding elements of  $x$ . More details are at <http://CRAN.R-project.org>.

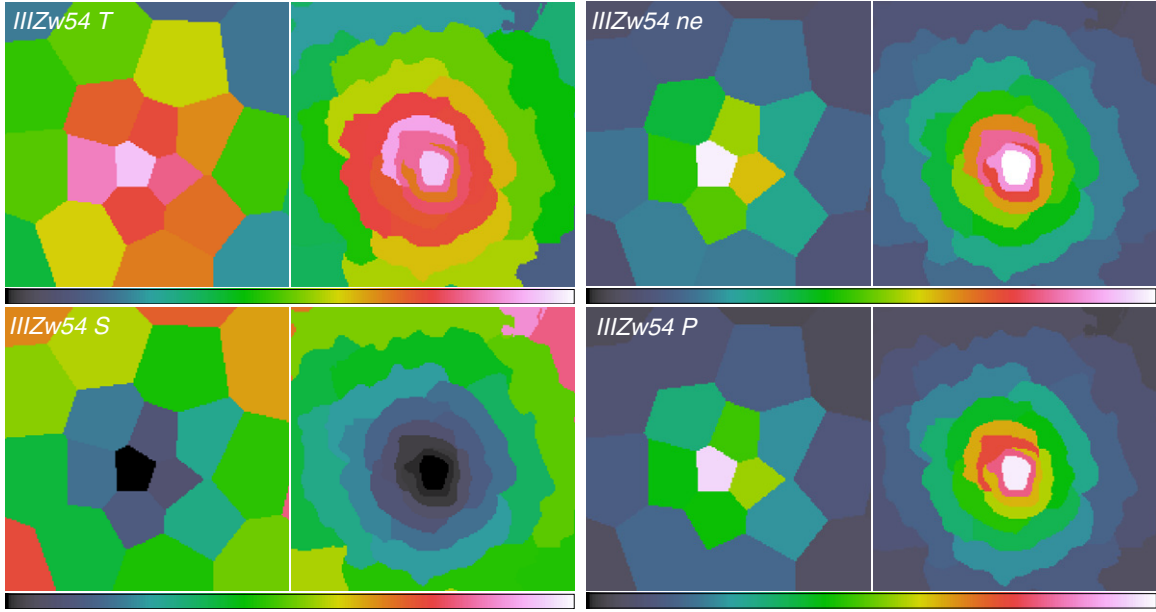


**Figure 5.** Temperature ( $T$ ), electron number density ( $n_e$ ), entropy ( $S$ ), and pressure ( $P$ ) maps for III Zw 54 with the *Mask-V* on the left and the *Mask-S* on the right in each panel. The color bars are in the range of 1.5–3.2 keV, 0–0.0063  $\text{cm}^{-3}$ , 90–400  $\text{keV cm}^2$ , and 0–0.02  $\text{keV cm}^{-3}$  in the  $T$ ,  $n_e$ ,  $S$ , and  $P$  panels, respectively. The image size is  $11' \times 11'$ .

(A color version of this figure is available in the online journal.)

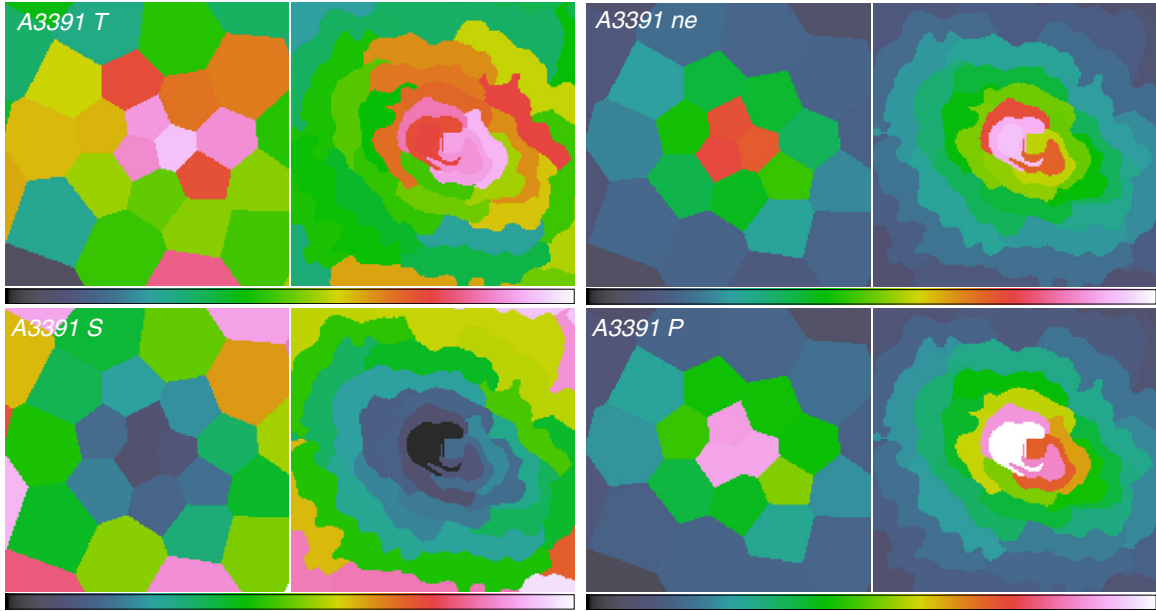


**Figure 6.** Temperature ( $T$ ), electron number density ( $n_e$ ), entropy ( $S$ ), and pressure ( $P$ ) maps for A3391 with the *Mask-V* on the left and the *Mask-S* on the right in each panel. The color bars are in the range of 3.3–6.5 keV, 0–0.0046  $\text{cm}^{-3}$ , 200–850  $\text{keV cm}^2$ , and 0–0.025  $\text{keV cm}^{-3}$  in the  $T$ ,  $n_e$ ,  $S$ , and  $P$  panels, respectively. The image size is  $11' \times 11'$ .

(A color version of this figure is available in the online journal.)

absolute fluctuation  $F_i$  is the area  $w_i$  of the corresponding  $i$ th spatial bin in the 2D map. The cumulative scatter and error are calculated from the area weighted absolute fluctuations as  $\sqrt{\sum F_i^2 w_i} / \sqrt{\sum w_i}$ , with all bins within  $d$ . The differential scatter and error are calculated from the weighted absolute fluctuations with all bins in the range of  $d_1$  and  $d_2$ , in which  $d = 0.5(d_1 + d_2)$ .

## 6.2. Scatter Profiles from the Azimuthal Average

When one single azimuthally averaged profile ( $D(d)$ ) for the four clusters as a whole is used, the scatter and error can indicate the degree of self-similarity of the investigated azimuthally

averaged quantities. We thus carry out a nonparametric fit on the scaled distribution of temperature, electron number density, entropy, and pressure, respectively, for the four clusters as a whole (see Figure 9). The cumulative scatter and error for the four clusters as a whole are shown in Figure 10, and the differential scatter and error are shown in Figure 11. The highest amplitude occurs in the cluster core ( $\leq 0.3r_{500}$ ) which is caused by the known difference between cool core and non-cool core clusters.

To avoid the above scatter due to the difference between cool core and non-cool core clusters in substructure diagnostics, we carry out a nonparametric fit to the scaled distribution of temperature, electron number density, entropy,

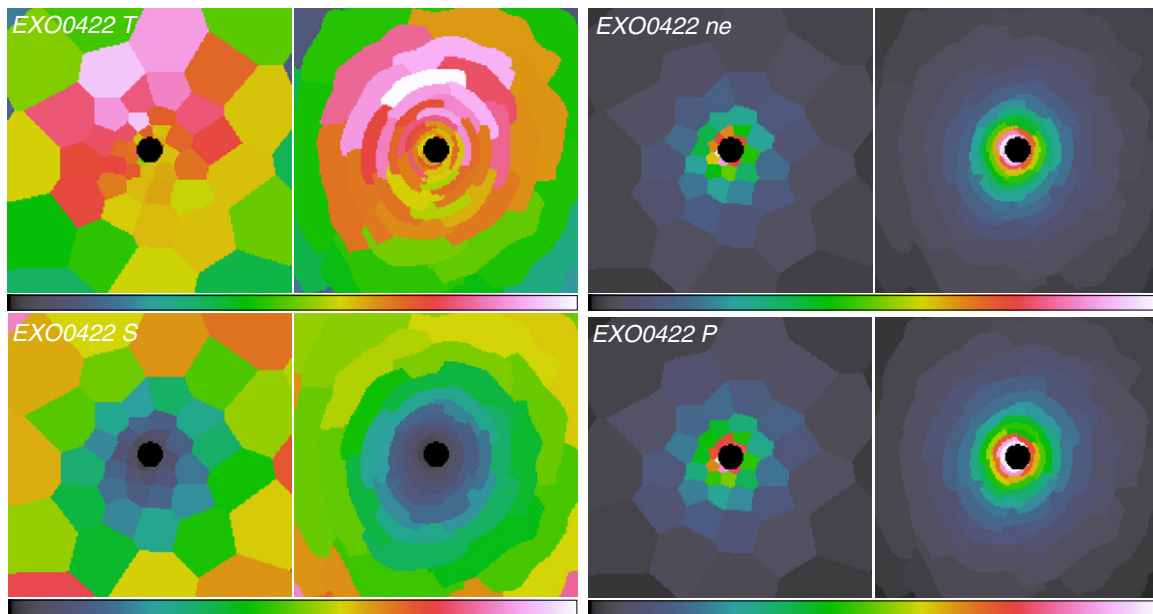


**Figure 7.** Temperature ( $T$ ), electron number density ( $n_e$ ), entropy ( $S$ ), and pressure ( $P$ ) maps for EXO0422 with the *Mask-V* on the left and the *Mask-S* on the right in each panel. The color bars are in the range of 1.5–4.2 keV, 0–0.023  $\text{cm}^{-3}$ , 20–580  $\text{keV cm}^2$ , and 0–0.025  $\text{keV cm}^{-3}$  in the  $T$ ,  $n_e$ ,  $S$ , and  $P$  panels, respectively. The image size is  $11' \times 11'$ . The hole in the cluster center for EXO0422 is the region excluded in the spectral analysis to avoid the possible contamination from the galaxy CIG0422-09 found by Belsole et al. (2005).

(A color version of this figure is available in the online journal.)

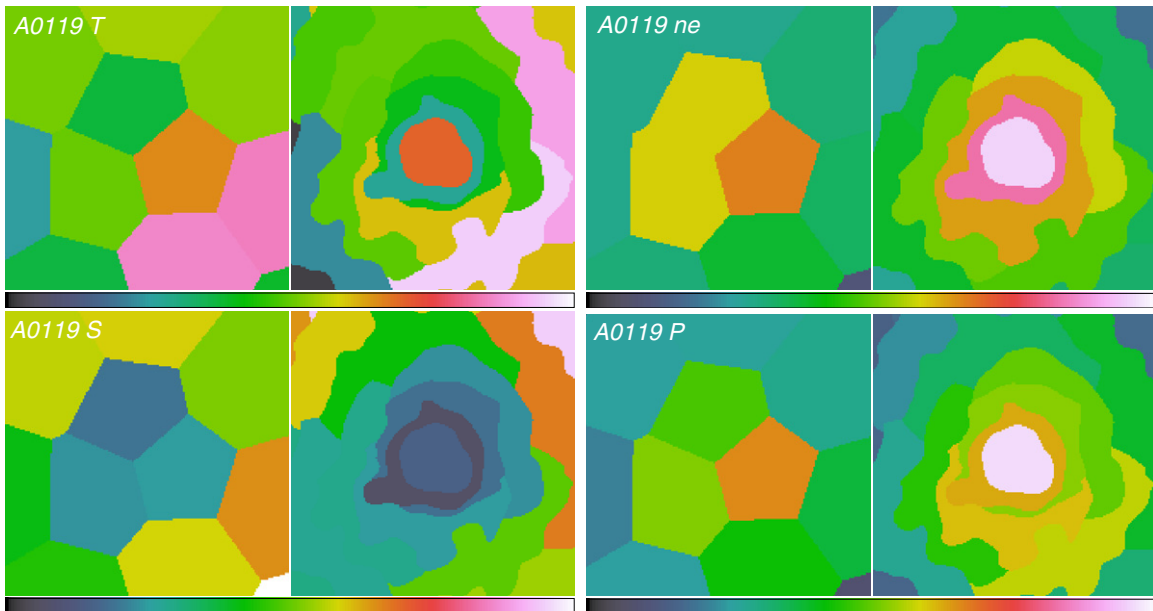


**Figure 8.** Temperature ( $T$ ), electron number density ( $n_e$ ), entropy ( $S$ ), and pressure ( $P$ ) maps for A0119 with the *Mask-V* on the left and the *Mask-S* on the right in each panel. The color bars are in the range of 3.5–7.2 keV, 0–0.003  $\text{cm}^{-3}$ , 200–900  $\text{keV cm}^2$ , and 0–0.018  $\text{keV cm}^{-3}$  in the  $T$ ,  $n_e$ ,  $S$ , and  $P$  panels, respectively. The image size is  $11' \times 11'$ .

(A color version of this figure is available in the online journal.)

and pressure, respectively, for each cluster to derive its own azimuthally averaged scaled distribution ( $\langle D(d) \rangle$ ). The cumulative scatter and error for the four clusters as a whole using the individual cluster mean scaled profiles are shown in Figure 12, and the differential scatter and error are shown in Figure 13. The cumulative scatter is quite flat. Its amplitude indicates  $\sim 10\%$  fluctuations in the temperature, electron number density, and entropy maps, and  $\sim 15\%$  fluctuations in the pressure map. The cumulative scatter and error for each cluster using the individual cluster mean scaled profiles are shown in Figure 14, and the differential scatter and error are shown in Figure 15.

To derive the mean profiles for each cluster, broader bins (a bin size of  $0.2r_{500}$ ) are used due to decreased statistics for individual clusters compared with the statistics for the four clusters as a whole, where we use a bin size of  $0.1r_{500}$ . The scatter here can be used as substructure diagnostics for individual clusters as shown in Section 6.3.

### 6.3. Substructure Diagnostics in Individual Clusters

A disturbance in the clusters appears as a high amplitude of and/or a discontinuity in the radial profile of the scatter of the fluctuations. The radial studies of the scatter of the fluctuations

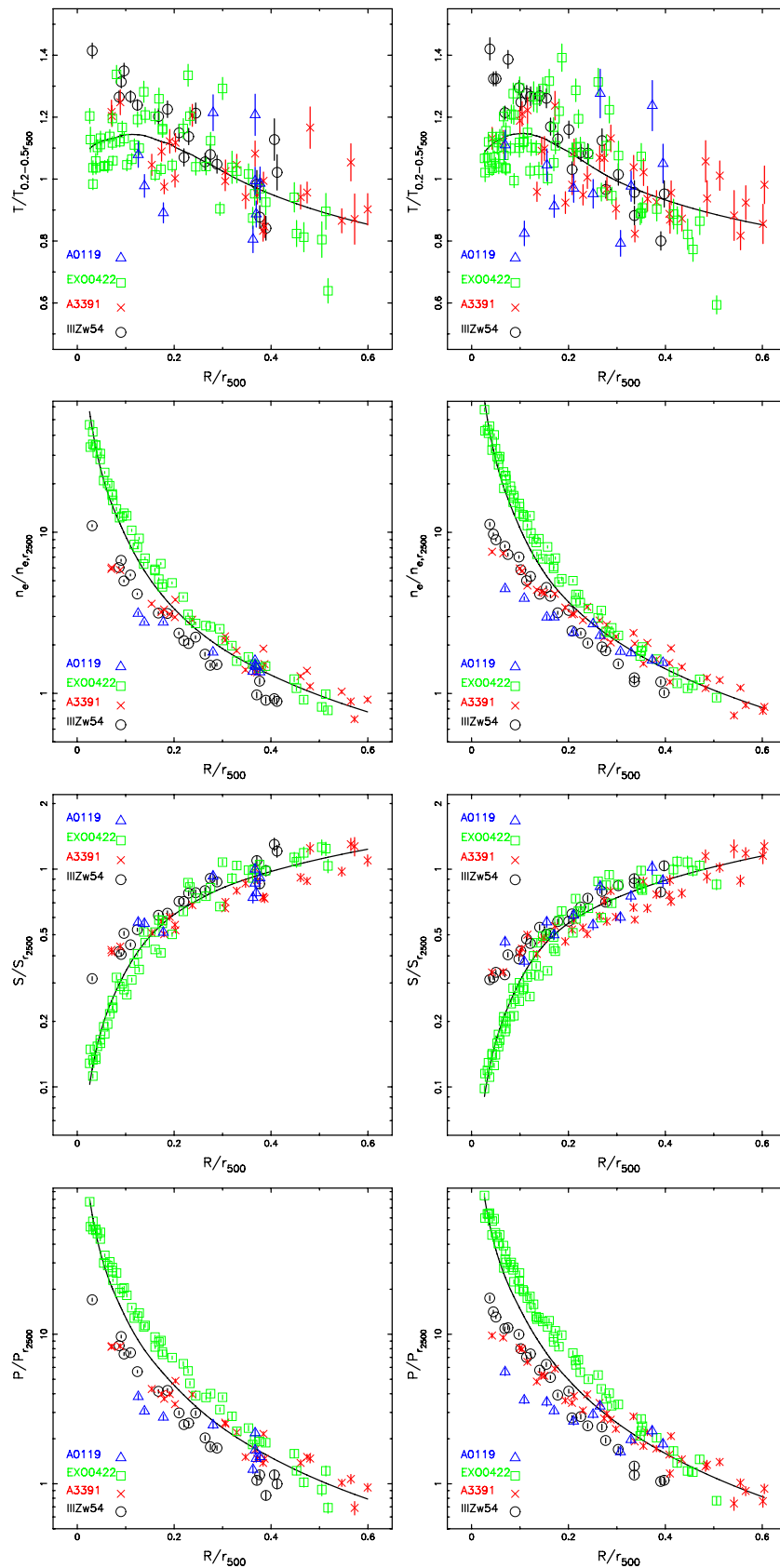


**Figure 9.** Normalized temperature, electron number density, entropy, and pressure distributions (from top to bottom) of the spectrally measured 2D maps using *Mask-V* (left) and *Mask-S* (right), respectively. The curves are the local regression fits of the distributions of the four clusters as a whole. (A color version of this figure is available in the online journal.)

in the 2D map for individual clusters thus provide detailed diagnostics to identify the ICM substructures.

*III Zw 54.* The 2D maps ( $T$ ,  $n_e$ ,  $S$ , and  $P$ ) show an azimuthally symmetric appearance (Figure 5). It has a relatively low am-

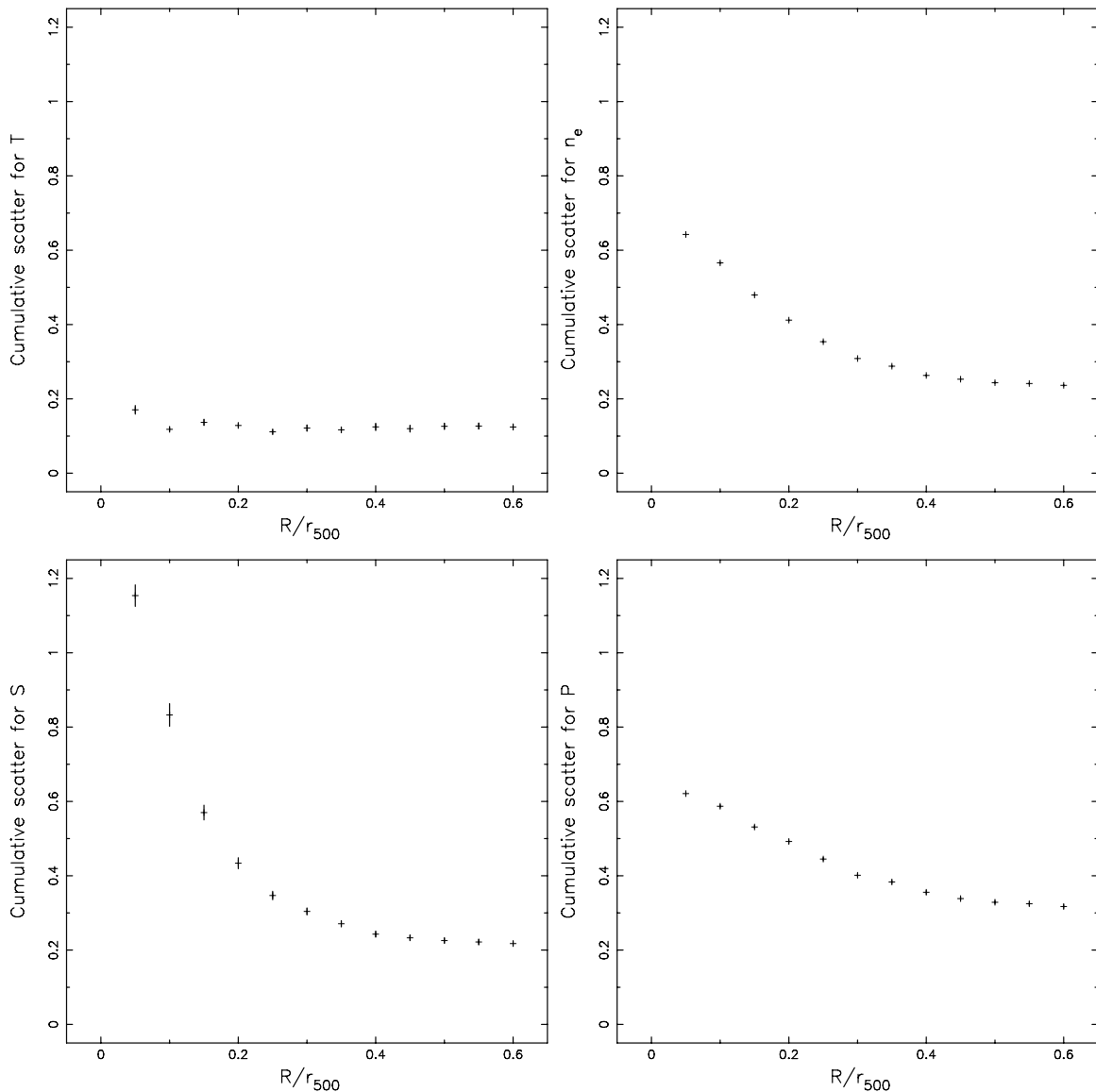


**Figure 10.** Cumulative scatter of the temperature, electron number density, entropy, and pressure fluctuations in the 2D maps for the four clusters as a whole using *Mask-S*. Note that for each plot, the mean profile  $\langle D(d) \rangle$  is determined for the four clusters as a whole as described in Section 6.2.

plitude of the scatter, particularly for the temperature and entropy fluctuations ( $\sim 5\%$ , see Figure 14). The cumulative scatter appears very flat. The differential scatter (Figure 15), which describes the local fluctuations, shows an increase for the temperature and entropy in the radial ranges beyond  $0.3r_{500}$  using the *Mask-V* only. This indicates that the substructure is roughly round clumps detectable using the *Mask-V* instead of isophotal annuli detectable using the *Mask-S*. Both the radial studies of the scatter and the 2D map appearance shows III Zw 54 is the most relaxed cluster among the four clusters, with mild entropy clumps beyond  $0.3r_{500}$ . It is peculiar that this cluster does not host a cool core (Figure 2). III Zw 54 therefore is an example of a relaxed non-cool core cluster.

*A3391*. It shows a mild increasing amplitude (from 4% to 10%) with radius in the cumulative scatter of the fluctuations (Figure 14). The electron number density and pressure scatter profiles show a discontinuity around  $0.2r_{500}$  using the *Mask-V*, at which radius the metallicity also shows significant clumps as well. It has an elliptically shaped morphology with a bisector feature divided by the short axis of the elliptical as shown in

Figure 6. It is known that A3391 is close to the interacting cluster A3395. The sector west of the cluster core up to  $\sim 0.25r_{500}$  shows  $\sim 1$  keV higher temperature, together with low electron number density, higher entropy, and low pressure in the maps (Figure 6). These substructure features are consistent with the observed discontinuity around  $0.2r_{500}$ , and all would suggest that some merging activities are present. A3391 is therefore an unrelaxed non-cool core cluster. The estimates of both the X-ray observables and the X-ray cluster mass for such an unrelaxed cluster can be biased due to the observed substructure.

*EXO0422*. This cluster shows the second highest scatter amplitude, particularly for the entropy. This is somewhat surprising because the X-ray surface brightness appears azimuthally symmetric and the radial temperature profile even shows a drop toward the center (Figure 2), typical of a cool core cluster. However, the temperature maps (Figure 7) clearly show a bisector feature divided by the southeast–northwest axis through the cluster core. The northeastern sector shows  $\sim 0.5$ – $1$  keV higher temperature and  $0.3$ – $0.5 Z_{\odot}$  higher metallicity than the southwestern sector. This feature might cause a high cluster tempera-

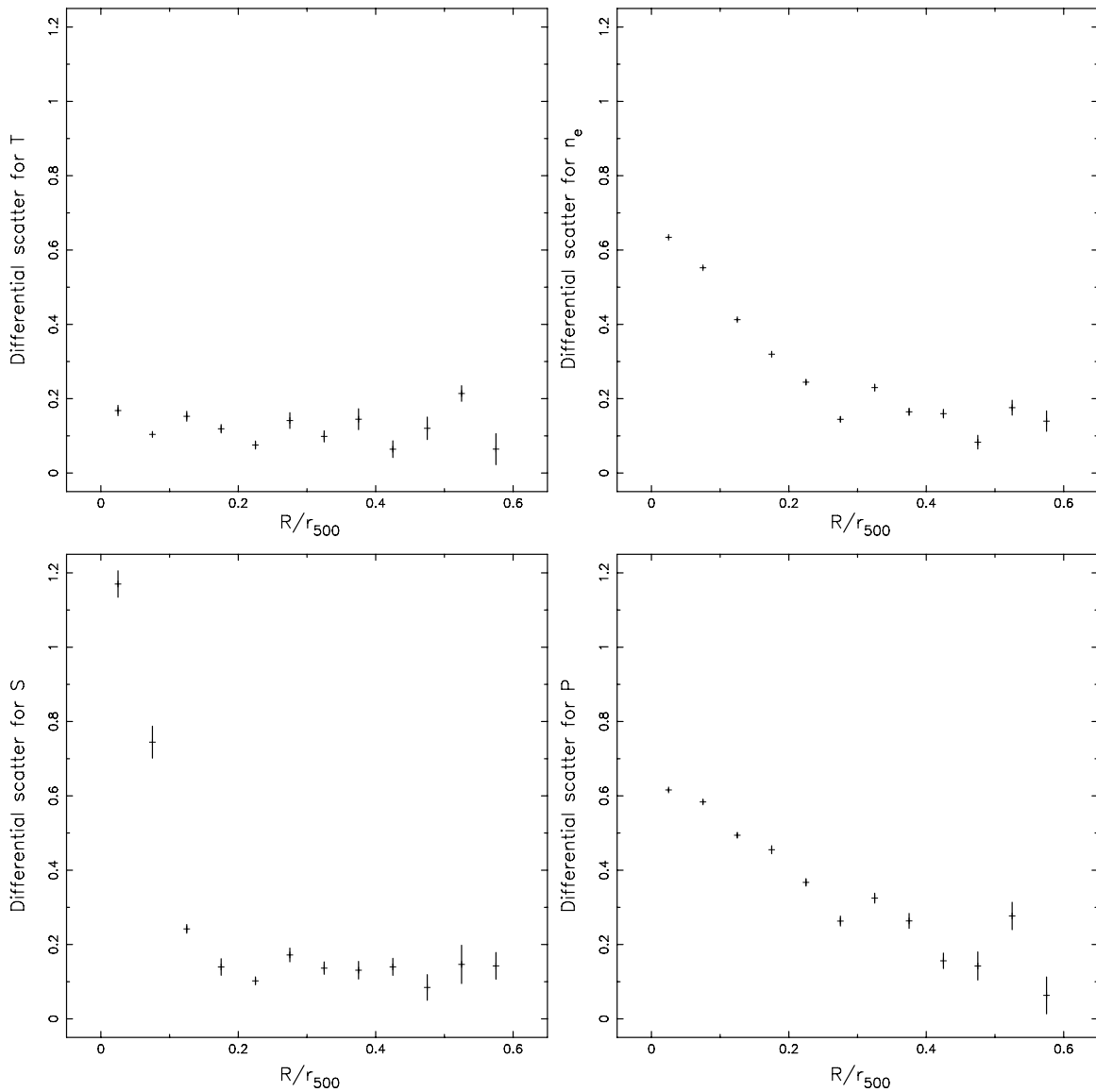


**Figure 11.** Differential scatter of the temperature, electron number density, entropy, and pressure fluctuations in the 2D maps for the four clusters as a whole using *Mask-S*. Note that for each plot, the mean profile  $\langle D(d) \rangle$  is determined for the four clusters as a whole as described in Section 6.2.

ture estimate, and thus a high  $Y_X$  parameter value. However, no such significant substructure features are shown in the electron number density, entropy, and pressure maps. This indicates the cluster is almost relaxed and that the total mass estimate for this cluster can hardly be biased. Therefore, EXO0422 is an almost relaxed cool core cluster. This seems to be a good example of a cluster with some merging activities which would go unnoticed without a temperature map. The scatter of the mass–observable relations for such an almost relaxed cluster can be caused by the bias in its temperature estimate and thus in its  $Y_X$  estimate due to the temperature substructure.

*A0119.* It stands out clearly in radial studies of the scatter in Figures 14 and 15. The scatter of the temperature fluctuations exhibits a high amplitude, particularly in the outskirts. We observe an elongation in its X-ray morphology with a faint emission tail (see also Buote & Tsai 1996; Hudson et al. 2009). Though this cluster has low-quality data, the maps show clearly an asymmetric structure with the southwestern sector up to 1–2 keV hotter than the northeastern sector

(Figure 8), and the high-temperature zone is located at a central radius of  $\sim 2'$  ( $\sim 0.17r_{500}$ ) from the cluster center using the *Mask-S* method. As the  $<0.2r_{500}$  region is excluded in the cluster temperature determination, the cluster temperature, and thus the  $Y_X$  parameter, is less affected by the hot structure in the cluster core. The pressure map shows a similar feature observed in the temperature map, while the entropy map shows less significant features. This suggests that the fluctuations of temperature and density are likely isentropic, which can be produced by a low Mach number shock, compression wave, turbulence, or triaxiality in the dark matter distribution. The appearance of A0119 is in favor of being unrelaxed. Its total mass estimate may thus be significantly affected. A0119 is an unrelaxed non-cool core cluster.

*Summary.* The application of the diagnostics on the four clusters shows the differential scatter of either entropy or temperature is a sensitive indicator of the substructure. Particularly, the temperature map is more sensitive to unnoticed substructure which only exists in the temperature map for an almost

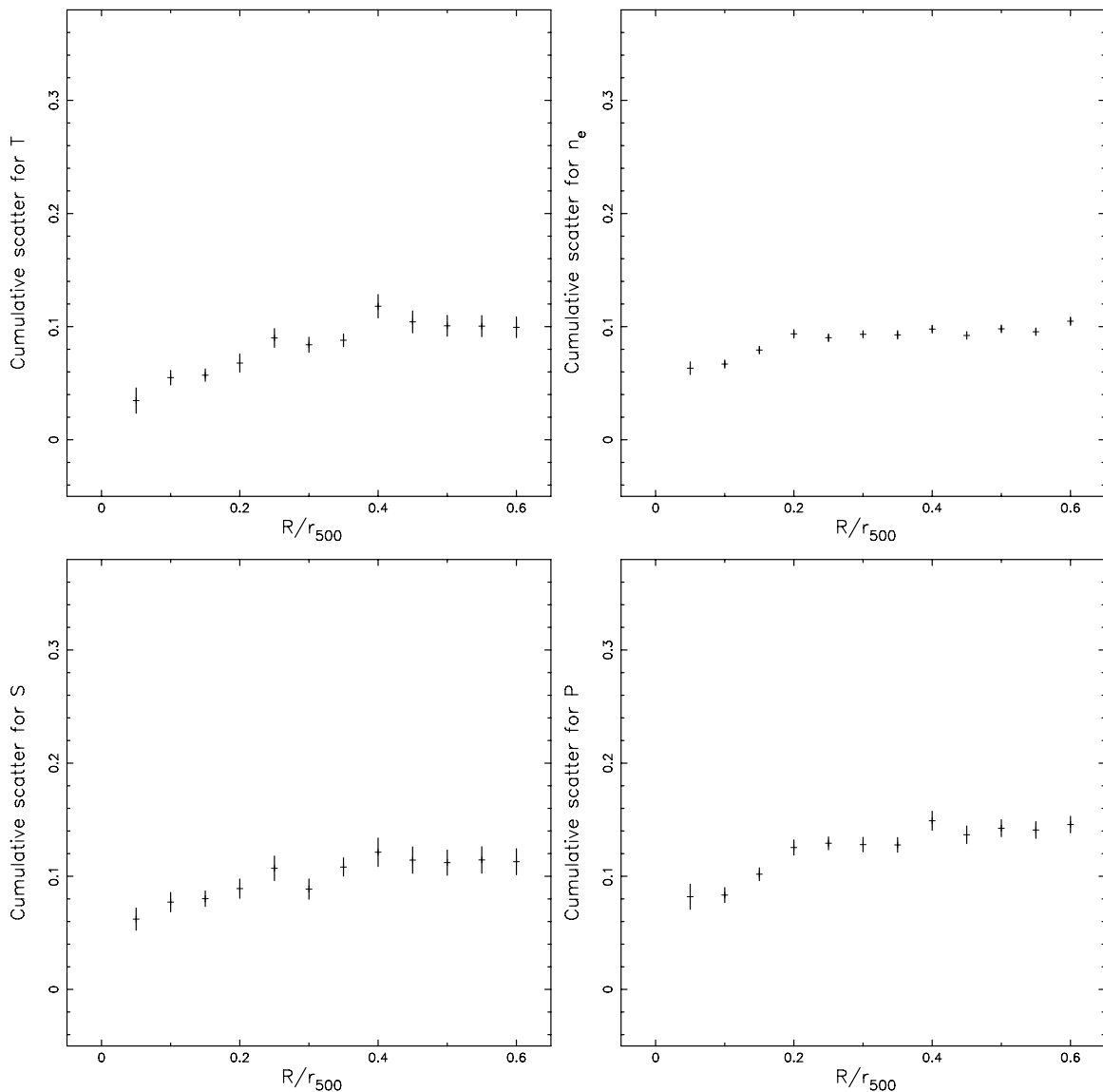


**Figure 12.** Cumulative scatter of the temperature, electron number density, entropy, and pressure fluctuations in the 2D maps for the four clusters as a whole using *Mask-S*. Note that for each plot, the mean profile  $\langle D(d) \rangle$  is individually determined for each cluster as described in Section 6.2.

relaxed cluster. For an unrelaxed cluster, the amplitudes of the scatter profiles in the 2D maps are likely high, with a possible discontinuity in the scatter profiles.

#### 6.4. Density versus Temperature Fluctuations

A correlation between temperature fluctuations and electron number density fluctuations may shed light on the origin of the fluctuations, e.g., a constant pressure solution yielding ratios of temperature fluctuations to electron number density fluctuations,  $-1$ ; and a constant entropy solution yielding ratios,  $2/3$ .

To check whether the electron number density fluctuations show a correlation with the temperature fluctuations, we performed a linear fit ( $Y = A + BX$ ) to the relation. It shows the highest Pearson correlation coefficient value for A0119 (Table 2), but is still hard to conclude a concrete correlation. There is no trend of the fluctuations as a function of radius except for a bump at radii of  $0.35\text{--}0.45r_{500}$  for the two unrelaxed clusters, A3391 and A0119.

#### 6.5. Scaling Relations versus ICM $T$ , $n_e$ , $S$ , and $P$ Fluctuations

The substructure diagnostics of galaxy clusters are of prime importance to the understanding of the X-ray mass estimates and the X-ray observables. In Zhang et al. (2008), we found the X-ray gas mass ( $M_{\text{gas}}$ ) and the X-ray analog of the integrated SZ flux ( $Y_X = M_{\text{gas}} \cdot T_{0.2\text{--}0.5r_{500}}$ ) can be used as low scatter cluster mass indicators compared with other X-ray observables. Therefore, we present the mass- $Y_X$  relation and mass- $M_{\text{gas}}$  relation here (Figure 16).

In simulations, there is a small intrinsic dispersion between the true mass and the mass derived from the hydrostatic equilibrium equation for relaxed clusters (e.g., Nagai et al. 2007). We therefore used the deviation of the cluster mass from the mass-observable relations for a sample of relaxed clusters as an indicator of the mass bias for the hydrostatic mass. Note that the mass-observable relations for relaxed clusters could still be biased by residual nonthermal support (e.g., Mahdavi et al. 2008; Zhang et al. 2008).

We have compiled a sample of 44 LoCuSS clusters (37 in Zhang et al. 2008), and used the best-fit scaling relations of the

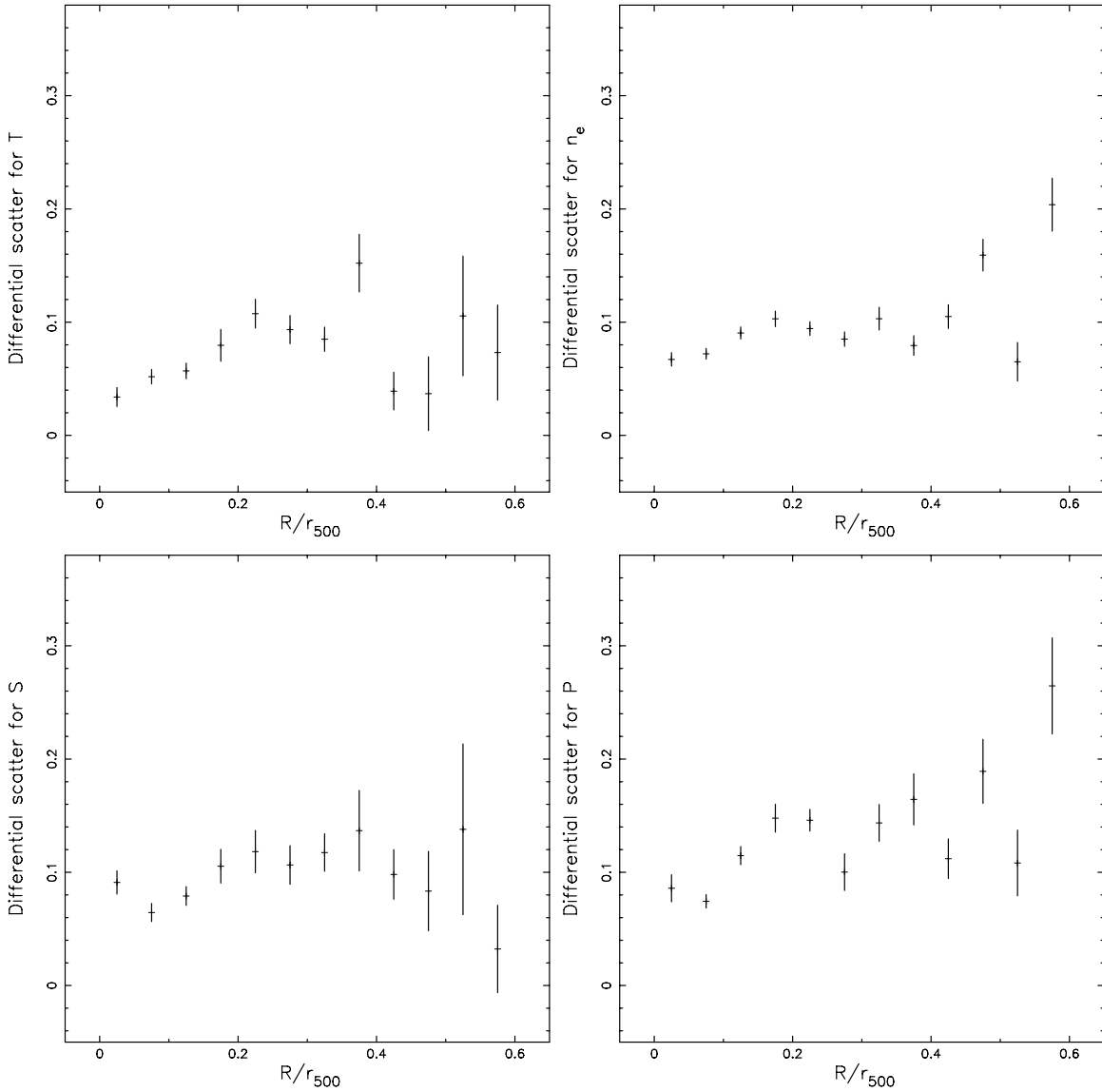


**Figure 13.** Differential scatter of the temperature, electron number density, entropy, and pressure fluctuations in the 2D maps for the four clusters as a whole using *Mask-S*. Note that for each plot, the mean profile  $\langle D(d) \rangle$  is individually determined for each cluster as described in Section 6.2.

**Table 2**

The Best Linear Fit ( $Y = A + BX$ ) of the Relation of Electron Number Density Fluctuations versus Temperature Fluctuations

Name	<i>Mask-V</i>			<i>Mask-S</i>		
	A	B	Coefficient	A	B	Coefficient
IIIZw54	$0.029 \pm 0.004$	$0.03 \pm 0.08$	0.154	$0.026 \pm 0.002$	$0.05 \pm 0.03$	0.321
A3391	$0.038 \pm 0.003$	$0.06 \pm 0.03$	0.335	$0.043 \pm 0.003$	$0.05 \pm 0.03$	0.285
EXO0422	$0.028 \pm 0.002$	$0.01 \pm 0.02$	0.066	$0.029 \pm 0.001$	$0.03 \pm 0.02$	0.323
A0119	$0.046 \pm 0.003$	$0.06 \pm 0.02$	0.765	$0.052 \pm 0.003$	$0.08 \pm 0.02$	0.830
All four clusters	$0.032 \pm 0.001$	$0.03 \pm 0.02$	0.192	$0.034 \pm 0.001$	$0.04 \pm 0.01$	0.263

subsample of all 22 relaxed clusters as the reference. At  $r_{2500}$ , the four clusters are in good agreement with the subsample of 22 relaxed LoCuSS clusters. With the cluster masses determined in Section 4, we observe tantalizing hints linking the scatter of the ICM fluctuations and the hydrostatic mass bias relative to the expected mass based on the  $M-Y_X$  and  $M-M_{\text{gas}}$  relations, particularly at  $r_{500}$ .

A typical example of a relaxed cluster, IIIZw54 (Figure 5), lies on the mass–observable scaling relations. A3391 is a weakly merging cluster (Figure 6), and lies significantly off

from the mass–observable scaling relations. EX0422 is a mild unrelaxed cool core cluster. Though its pressure map has no significant substructures which means the cluster mass may be unbiased. The hot substructure in the temperature map could cause a high cluster temperature estimate and thus a high  $Y_X$  estimate. As a result, it lies on the mass– $M_{\text{gas}}$  scaling relations but shows a small offset toward the hot side in the  $M-Y_X$  relation, particularly at  $r_{500}$ . A typical example of a dynamically active cluster is A0119 (Figure 8). The significant feature of substructures observed in the pressure map might cause a

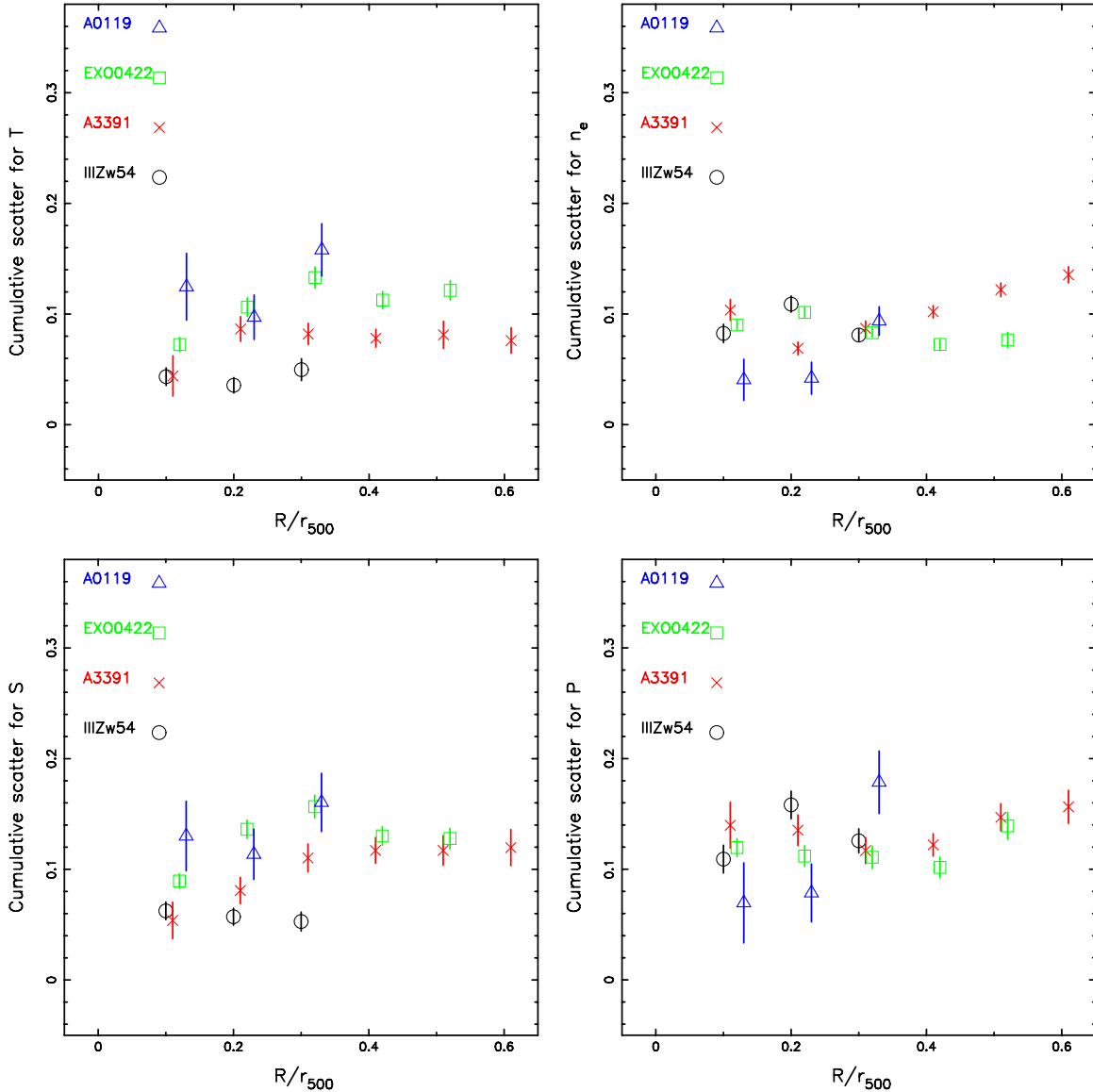


**Figure 14.** Cumulative scatter of the temperature, electron number density, entropy, and pressure fluctuations in the 2D maps for each cluster using *Mask-S*. The X-axis has been shifted by 0.005, 0.010, and 0.015 for A3391, EXO0422, and A0119, respectively, to avoid the overlap. Note that for each plot, the mean profile  $\langle D(d) \rangle$  is individually determined for each cluster as described in Section 6.2.

(A color version of this figure is available in the online journal.)

large bias in the cluster mass estimate. This cluster indeed shows significant deviations in both the  $M$ – $Y_X$  and  $M$ – $M_{\text{gas}}$  relations.

To quantify the trend between the mass bias and the scatter of the fluctuations in the 2D maps, we defined the quasi-mass bias as follows. For example, the quasi-true mass  $M_{\Delta}^{Y_X}$  (or  $M_{\Delta}^{M_{\text{gas}}}$ ) can be derived from  $Y_X$  (or  $M_{\text{gas}}$ ) at  $r_{\Delta}$  via the  $M_{\Delta}$ – $Y_X$  (or  $M_{\Delta}$ – $M_{\text{gas}}$ ) scaling relation of a subsample of 22 LoCuSS clusters characterized as relaxed. The quasi-mass bias is thus defined as  $B_{M_{\Delta}}^{Y_X} = M_{\Delta}/M_{\Delta}^{Y_X} - 1$  (or  $B_{M_{\Delta}}^{M_{\text{gas}}} = M_{\Delta}/M_{\Delta}^{M_{\text{gas}}} - 1$ ). We carried out a simple linear fit  $Y = A + BX$  to the relation of the quasi-mass bias at  $r_{\Delta}$  versus the cumulative scatter at the outermost radius one can measure for individual clusters. The correlation is only significant (i.e., correlation coefficient  $> 0.65$ ) using the scatter of either entropy or pressure fluctuations and using the quasi-mass bias at  $r_{500}$ . Therefore, we only list the best fit and Pearson correlation coefficient using the scatter of entropy, and pressure fluctuations and the quasi-mass bias at  $r_{500}$

in Table 3. We interpret this result as tentative evidence for an interesting correlation between mass bias and scatter amplitude. We will constrain the parameters of these relations in more detail using a larger cluster sample. These findings shall encourage similar studies to be carried out using hydrodynamical simulations.

#### 6.6. Data Quality versus Radial Studies of ICM $T$ , $n_e$ , $S$ , and $P$ Fluctuations

As shown above, sufficient photon statistics are required to provide quantitative diagnostics of the substructure in the ICM and to imply detailed physics relevant to the systematics of the scaling relations. EXO0422 has the highest data quality among the four clusters. Therefore, the ICM substructure shown in great details allows us to understand its small offset in the scaling relations, which would have been missed without our studies. A0119 has insufficient photon statistics to perform such radial studies of the ICM  $T$ ,  $n_e$ ,  $S$ , and  $P$  fluctuations. Though

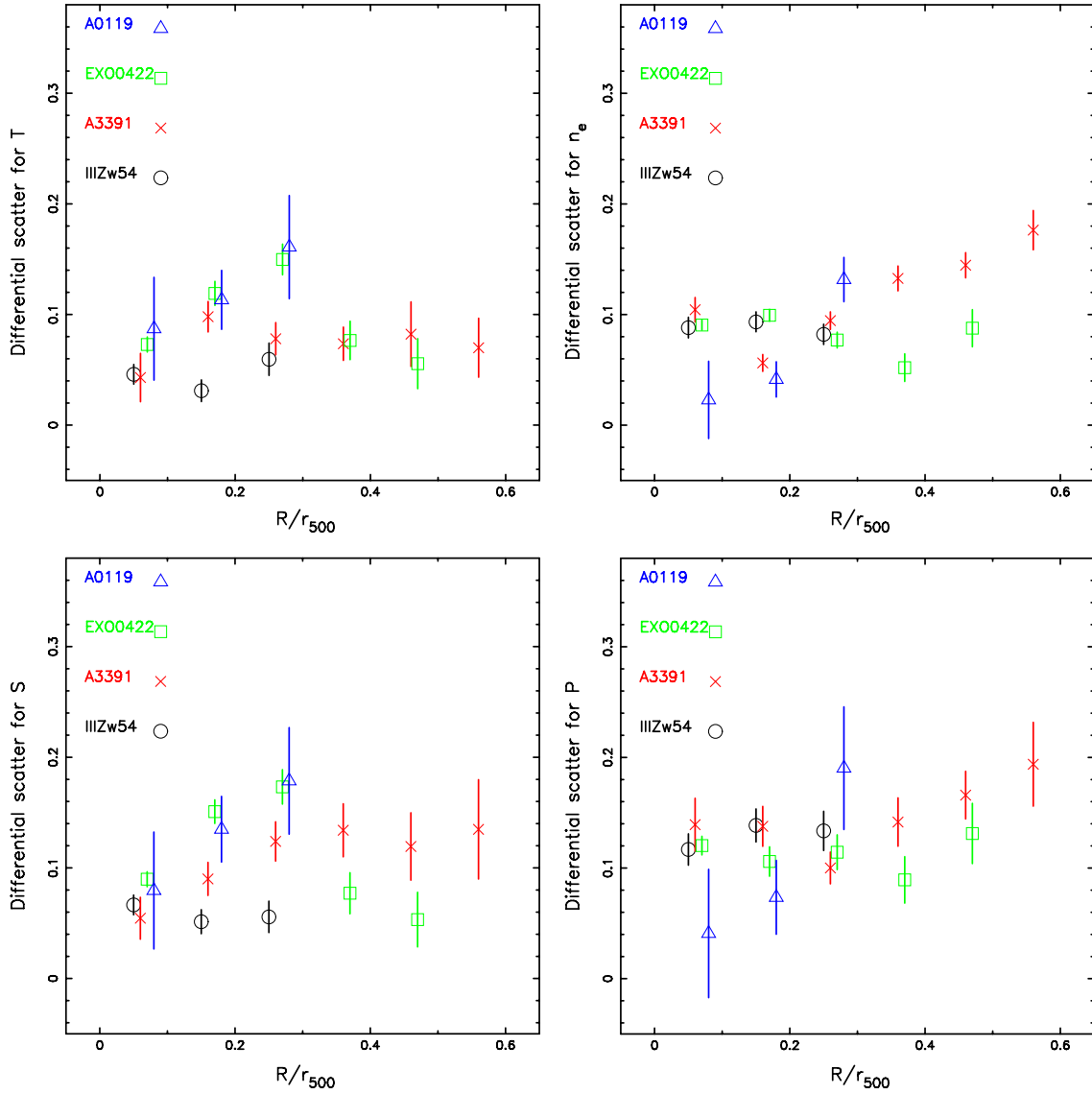


**Figure 15.** Differential scatter of the temperature, electron number density, entropy, and pressure fluctuations in the 2D maps for each cluster using *Mask-S*. The X-axis has been shifted by 0.005, 0.010, and 0.015 for A3391, EXO0422, and A0119, respectively, to avoid the overlap. Note that for each plot, the mean profile  $\langle D(d) \rangle$  is individually determined for each cluster as described in Section 6.2.

(A color version of this figure is available in the online journal.)

**Table 3**

The Best Linear Fit ( $Y = A + BX$ ) of the Relation of the Quasi-Mass Bias, Column (1), versus the Cumulative Scatter at the Outermost Radius One can Measure for Individual Clusters, Column (2)

Bias	Scatter	<i>Mask-V</i>			<i>Mask-S</i>		
		<i>A</i>	<i>B</i>	Coefficient	<i>A</i>	<i>B</i>	Coefficient
$B_{M500}^{YX}$	<i>S</i>	$1.45 \pm 0.38$	$-14.3 \pm 3.3$	-0.98	$0.61 \pm 0.22$	$-6.6 \pm 1.9$	-0.80
	<i>P</i>	$1.07 \pm 0.29$	$-8.0 \pm 1.9$	-0.97	$1.12 \pm 0.31$	$-9.2 \pm 2.2$	-0.97
$B_{M500}^{M_{\text{gas}}}$	<i>S</i>	$1.06 \pm 0.41$	$-9.8 \pm 3.6$	-0.95	$0.42 \pm 0.23$	$-4.0 \pm 2.0$	-0.69
	<i>P</i>	$0.79 \pm 0.32$	$-5.5 \pm 2.1$	-0.94	$0.76 \pm 0.32$	$-5.9 \pm 2.3$	-0.90

**Note.** See details in Section 6.5.

we observed significant features indicating the strong merging activities in the 2D maps of A0119, the radial profiles of the scatter show large statistical error and could not reveal possible discontinuities. Therefore,  $\geq 30$  bins within the  $0.6r_{\text{tr}}$  region is required for such radial studies of the fluctuations of the spectrally measured ICM  $T$ ,  $n_e$ ,  $S$ , and  $P$  maps. In term of net counts,  $\geq 120,000$  cluster photons are required for one nearby cluster.

## 7. CONCLUSIONS

Substructure diagnostics of galaxy clusters are crucial to the robustness of the estimates of both the cluster mass and the X-ray observables. Therefore, they have enormous importance to the understanding of the systematics and scatter of the mass-observable scaling relations. As a result, the knowledge of the substructure directly affects the precision of the cosmological

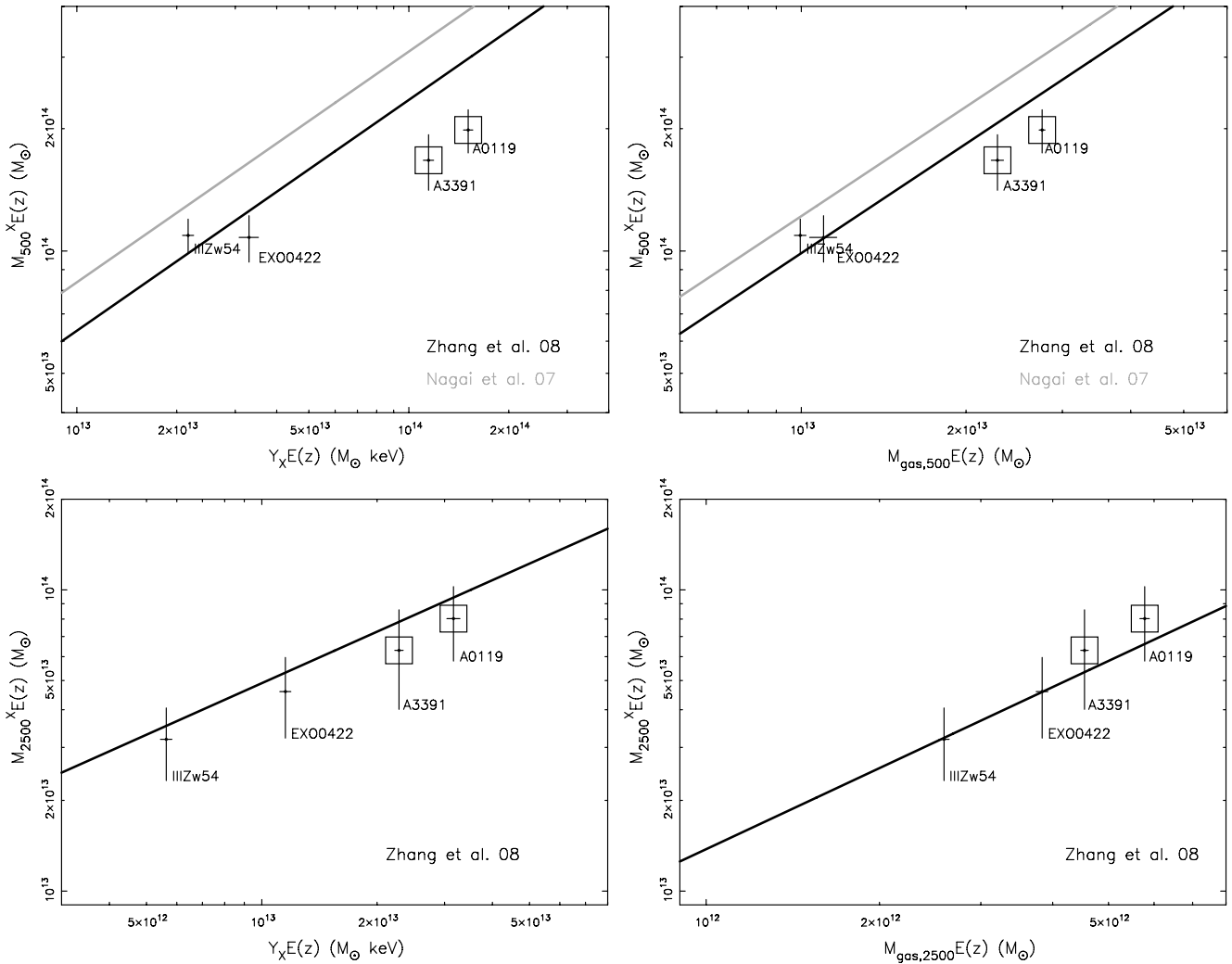


**Figure 16.** Mass– $Y_X$  relations (left) and the mass– $M_{\text{gas}}$  relations (right). We compile a sample of 44 LoCuSS clusters (37 LoCuSS clusters are from Zhang et al. 2008) and use the best-fit scaling relations of a subsample of 22 clusters characterized as relaxed (black lines) at  $r_{500}$  and  $r_{2500}$ , respectively, as the reference for our studies. The scaling relations at  $r_{500}$  from simulations in Nagai et al. (2007; gray lines) are shown for comparison. Clusters characterized as possibly merging/elliptical in Hudson et al. (2009) are denoted by open squares. The cluster masses for the four clusters are determined in Section 4.

tests using the cluster mass function. To probe possible biases in hydrostatic mass estimates as a function of cluster dynamical state, we developed a precise background subtraction procedure using both MOS and pn and a spectral analysis procedure to derive the X-ray maps via spectral measurements in each spatial bin. With *XMM-Newton* observations of the four morphological different clusters selected from the HIFLUGCS sample, we report our procedures and strategies for the ICM substructure studies using the spectrally measured 2D temperature, electron number density, entropy, and pressure maps with medium quality *XMM-Newton* data for nearby clusters. Our procedures provide detailed 2D diagnostics and a new complementary tool, the radial studies of the fluctuations in the 2D map of ICM temperature, electron number density, pressure, and entropy, to quantify the substructure in galaxy clusters, and attempt to explain the deviation of the cluster from the mass–observable scaling relations.

The amplitude of and the discontinuity in the scatter provide substructure diagnostics due to merging, the physics behind the scatter of the mass–observable scaling relations. The amplitude indicates  $\sim 10\%$  fluctuations in the temperature, electron number density, and entropy maps, and  $\sim 15\%$  fluctuations in the

pressure map. The differential scatter can indicate the most disturbed radial range, e.g.,  $0.35\text{--}0.45r_{500}$  for the unrelaxed clusters, A3391 and A0119.

The temperature map is particularly unique to identify the substructure of an almost relaxed cluster which would be unnoticed in the ICM electron number density and pressure maps.

There is a tantalizing link between the substructure identified using the scatter of the entropy and pressure fluctuations and the hydrostatic mass bias relative to the expected mass based on the  $M\text{--}Y_X$  and  $M\text{--}M_{\text{gas}}$  relations particularly at  $r_{500}$ . A typical relaxed cluster, such as III Zw 54, lies on the mass–observable scaling relations. A weakly merging cluster, A3391, lies significantly off from the mass–observable scaling relations. An almost relaxed cool core cluster, EXO0422, shows a small offset in the  $M\text{--}Y_X$  relation. A typical dynamical active cluster, A0119, shows significant mass deviation in the both  $M\text{--}Y_X$  and  $M\text{--}M_{\text{gas}}$  relations. The scatter of the observed scaling relations caused by an unrelaxed cluster can be due the mass estimate being biased by the pressure substructure and the temperature estimate biased by the temperature substructure in this cluster, e.g., A0119. The scatter of the observed scaling relations can

also be caused by an almost relaxed cluster, due to the bias in its temperature estimate affected by its temperature substructure, e.g., EXO0422.

*XMM-Newton* observations with  $\geq 120,000$  source photons per cluster are sufficient to apply our method for detailed diagnostics to identify the substructures of the clusters. More concrete conclusions require such substructure studies using a statistically large sample, with  $\geq 120,000$  source photons per cluster in their *XMM-Newton* observations; this is work in progress. It will then be interesting to make a detailed comparison of a possible scatter–mass bias correlation with the results of numerical simulations.

The *XMM-Newton* project is an ESA Science Mission with instruments and contributions directly funded by ESA Member States and the USA (NASA). The *XMM-Newton* project is supported by the Bundesministerium für Wirtschaft und Technologie/Deutsches Zentrum für Luft- und Raumfahrt (BMW/DLR, FKZ 50 OX 0001) and the Max-Planck Society. Y.Y.Z. acknowledges J. de Plaa, S. L. Snowden, H. Böhringer, and J. S. Sanders for useful discussions. Y.Y.Z., T.H.R., and D.S.H. acknowledge support by the DFG through Emmy Noether Research Grant RE 1462/2 and the Transregional Collaborative Research Centre TRR33 “The Dark Universe” and by the German BMBF through the Verbundforschung under grant 50 OR 0601. A.F. acknowledges support from BMBF/DLR under grant 50 OR 0207 and MPG and support through the funding of the DFG for the Excellence Cluster Universe EXC153. C.L.S. was supported in part by NASA *XMM-Newton* grants NNX06AE76G, NNX08AZ34G, and NNX08AW83G, and by *Chandra* grant GO7-8129X. This work has been partially supported from NASA grants NNX07AV73G and NNX07AT29G. For help in the early stage of the project, we acknowledge H. Böhringer, T. Clarke, T. Erben, A. Evrard, Y. Fujita, Y. Ikebe, O.-E. Nenestyan, E. Pierpaoli, S. Randall, and P. Schuecker.

## REFERENCES

- Allen, S. W., Schmidt, R. W., & Fabian, A. C. 2002, *MNRAS*, **334**, L11
- Anders, E., & Grevesse, N. 1989, *Geochim. Cosmochim. Acta*, **53**, 197
- Andersson, K., Peterson, J. R., Madejski, G. M., & Goobar, A. 2009, *ApJ*, **696**, 1029
- Arnal, E. M., et al. 2000, *A&AS*, **142**, 35
- Arnaud, M., Pointecouteau, E., & Pratt, G. W. 2007, *A&A*, **474**, L37
- Bajaja, E., et al. 2005, *A&A*, **440**, 767
- Becker, R. A., Chambers, J. M., & Wilks, A. R. 1988, *The New S Language* (Pacific Grove, CA: Wadsworth & Brooks)
- Belsole, E., Birkinshaw, M., & Worrall, D. M. 2005, *MNRAS*, **358**, 120
- Belsole, E., Pratt, G.W., Sauvageot, J.-L., & Bourdin, H. 2004, *A&A*, **415**, 821
- Beuermann, K. 2008, *A&A*, **481**, 919
- Boggs, P. T., Byrd, R. H., & Schnabel, R. B. 1987, *SIAM J. Sci. & Stat. Comput.*, **8**(6), 1052
- Böhringer, H., et al. 2004, *A&A*, **425**, 367
- Böhringer, H., et al. 2007, *A&A*, **469**, 363
- Buote, D. A., & Tsai, J. C. 1996, *ApJ*, **458**, 27
- Cappellari, M., & Copin, Y. 2003, *MNRAS*, **342**, 345
- Churazov, E., Forman, W., Jones, C., & Böhringer, H. 2003, *ApJ*, **590**, 225
- De Luca, A., & Molendi, S. 2004, *A&A*, **419**, 837
- de Plaa, N., et al. 2006, *A&A*, **452**, 397
- Diehl, S., & Statler, T. S. 2006, *MNRAS*, **368**, 497
- Ebeling, H., et al. 1998, *MNRAS*, **301**, 881
- Ebeling, H., et al. 2000, *MNRAS*, **318**, 333
- Evrard, A. E., Metzler, C. A., & Navarro, J. F. 1996, *ApJ*, **469**, 494
- Evrard, A. E., et al. 2008, *ApJ*, **672**, 122
- Fabian, A. C., Celotti, A., Blundell, K. M., Kassim, N. E., & Perley, R. A. 2002, *MNRAS*, **331**, 369
- Fabian, A. C., et al. 2001, *MNRAS*, **321**, L33
- Finoguenov, A., Böhringer, H., & Zhang, Y.-Y. 2005, *A&A*, **442**, 827
- Forman, W., et al. 2007, *ApJ*, **665**, 1057
- Freyberg, M. J., et al. 2006, The EPIC pn-CCD Detector Aboard *XMM-Newton* XMM-SOC-CAL-TN-0068 (Madrid: ESA), [http://xmm.esac.esa.int/cgi-bin/docs/DOC\\_list?Type=TN](http://xmm.esac.esa.int/cgi-bin/docs/DOC_list?Type=TN)
- Ghizzardi, S. 2001, In-Flight Calibration of the PSF for the MOS1 and MOS2 Cameras, EPIC-MCT-TN-011 (Madrid: ESA)
- Hartmann, D., & Burton, W. B. 1997, *Atlas of Galactic Neutral Hydrogen* (Cambridge: Cambridge Univ. Press)
- Henry, J. P., Finoguenov, A., & Briel, U. G. 2004, *ApJ*, **615**, 181
- Hudson, D. S., et al. 2009, *A&A*, submitted.
- Jee, M. J., & Tyson, J. A. 2009, *ApJ*, **691**, 1337
- Jia, S.-M., Böhringer, H., Pointecouteau, E., Chen, Y., & Zhang, Y.-Y. 2008, *A&A*, **489**, 1
- Jones, C., & Forman, W. 1984, *ApJ*, **276**, 38
- Kalberla, P. M. W., et al. 2005, *A&A*, **440**, 775
- Kapferer, W., Kronberger, T., Ferrari, C., Riser, T., & Schindler, S. 2008, *MNRAS*, **389**, 1405
- Mahdavi, A., Hoekstra, H., Babul, A., & Henry, J. P. 2008, *MNRAS*, **384**, 1567
- Markevitch, M., Govoni, F., Brunetti, G., & Jerius, D. 2005, *ApJ*, **627**, 733
- Markevitch, M., Vikhlinin, A., & Mazzotta, P. 2001, *ApJ*, **562**, L153
- Markevitch, M., et al. 2003, *ApJ*, **586**, L19
- Nagai, D., Vikhlinin, A., & Kravtsov, A. 2007, *ApJ*, **688**, 1
- Piffaretti, R., & Valdarnini, R. 2008, *A&A*, **491**, 71
- Poole, G. B., Babul, A., & McCarthy, I. G. 2007, *MNRAS*, **380**, 437
- Poole, G. B., et al. 2006, *MNRAS*, **373**, 881
- Pratt, G. W., Böhringer, H., & Finoguenov, A. 2005, *A&A*, **433**, 777
- Reiprich, T. H., & Böhringer, H. 2002, *ApJ*, **567**, 716
- Reiprich, T. H., Sarazin, C. L., Kempner, J. C., & Tittley, E. 2004, *ApJ*, **608**, 179
- Reiprich, T. H., et al. 2009, *A&A*, in press (arXiv:0806.2920)
- Ricker, P. M., & Sarazin, C. L. 2001, *ApJ*, **561**, 621
- Riemer-Sorensen, S., et al. 2009, *ApJ*, **693**, 1570
- Sakelliou, I., & Ponman, T. J. 2006, *MNRAS*, **367**, 1409
- Sanders, J. S. 2006, *MNRAS*, **371**, 829
- Sanders, J. S., & Fabian, A. C. 2007, *MNRAS*, **381**, 1381
- Sanderson, A. J. R., Finoguenov, A., & Mohr, J. J. 2005, *ApJ*, **630**, 191
- Schuecker, P., Finoguenov, A., Miniati, F., Böhringer, H., & Briel, U. G. 2004, *A&A*, **426**, 387
- Sijacki, D., & Springel, V. 2006, *MNRAS*, **371**, 1025
- Simionescu, A., Böhringer, H., Brügggen, M., & Finoguenov, A. 2007, *A&A*, **465**, 749
- Smith, G. P., & Taylor, J. E. 2008, *ApJ*, **682**, L73
- Snowden, S. L., Mushotzky, R. F., Kuntz, K. D., & Davis, D. S. 2008, *A&A*, **478**, 615
- Sun, M., Donahue, M., & Voit, G. M. 2007, *ApJ*, **671**, 190
- Ventimiglia, D. A., Voit, G. M., Donahue, M., & Ameglio, S. 2008, *ApJ*, **685**, 118
- Vikhlinin, A., Markevitch, M., & Murray, S. S. 2001, *ApJ*, **549**, L47
- Vikhlinin, A., et al. 2006, *ApJ*, **640**, 691
- Vikhlinin, A., et al. 2009a, *ApJ*, **692**, 1033
- Vikhlinin, A., et al. 2009b, *ApJ*, **692**, 1060
- Zhang, Y.-Y., Böhringer, H., Mellier, Y., Soucail, G., & Forman, W. 2005, *A&A*, **429**, 85
- Zhang, Y.-Y., et al. 2004, *A&A*, **413**, 49
- Zhang, Y.-Y., et al. 2006, *A&A*, **456**, 55
- Zhang, Y.-Y., et al. 2007, *A&A*, **467**, 437
- Zhang, Y.-Y., et al. 2008, *A&A*, **482**, 451